Cooperative Sense and Avoid for UAVs using Secondary Radar

Mohammadkarimi, Mostafa; Rajan, Raj Thilak

DOI
10.1109/TAES.2024.3410953

Publication date
2024

Document Version
Final published version

Published in
IEEE Transactions on Aerospace and Electronic Systems

Cooperative Sense and Avoid for UAVs Using Secondary Radar

MOSTAFA MOHAMMADKARIMI, Member, IEEE
RAJ THILAK RAJAN, Senior Member, IEEE
Delft University of Technology, Delft, The Netherlands

A cooperative sense and avoid (SAA) algorithm for safe navigation of small-sized unmanned aerial vehicles (UAVs) within an airspace is proposed in this article. The proposed method relies upon cooperation between the UAV and the surrounding transponder-equipped aviation obstacles. To do so, the aviation obstacles share their altitude and identification code with the UAV by using the Mode S operation of the secondary surveillance radar (SSR) after interrogation. The proposed SAA algorithm benefits from the estimate of the aviation obstacle's elevation angle for ranging. This results in more accurate ranging compared to the round-trip time-based ranging, which is currently used in existing SAA systems. We also propose a low-complexity and accurate radial velocity estimator for the Mode S operation of the SSR, which is employed in the proposed SAA system. Furthermore, by considering the pulse-position modulation of the transponder reply as a waveform of pulse radar with random pulse repetition intervals, the maximum unambiguous radial velocity is obtained. The proposed SAA is equipped with an intruder identification method that determines the risk level of the surrounding transponder-equipped aviation obstacles. Given the estimated parameters, the intruder identification method classifies the aviation obstacles into high- medium-, and low-risk intruders. The output of the classifier enables the UAV to plan its path or maneuver for safe navigation accordingly. The root mean square error of the proposed estimators are analytically derived, and the effectiveness of our SAA solution is confirmed through simulation experiments.

Manuscript received 8 June 2023; revised 13 December 2023 and 24 March 2024; accepted 1 June 2024. Date of publication 7 June 2024; date of current version 11 October 2024.

DOI. No. 10.1109/TAES.2024.3410953

Refereeing of this contribution was handled by C. Clemente.

This work was supported in part by the European Leadership Joint Undertaking (ECSEL JU) under Grant 876019, and in part by the ADACORSA project—"Airborne Data Collection on Resilient System Architectures".

Authors' addresses: Mostafa Mohammadkarimi and Raj Thilak Rajan are with the Faculty of Electrical Engineering, Mathematics, and Computer Science, Delft University of Technology, 2628 CD Delft, The Netherlands, E-mail: (m.mohammadkarimi@tudelft.nl; R.T.Rajan@tudelft.nl). *(Corresponding author: Mostafa Mohammadkarimi.)*

NOMENCLATURE

List of Acronyms and Symbols

ACAS	Airborne collision avoidance system.
ADC	Analog-to-digital converter.
AOA-E	Angle-of-arrival estimator.
AV	Aerial vehicle.
AWGN	Additive white Gaussian noise.
CRC	Cyclic redundancy check.
MAV	Manned aerial vehicle.
MUSIC	Multiple Signal Classification.
NC-SD	Noncoherent symbol detector.
PPM	Pulse-position modulation.
PSD	Power spectral density.
PRI	Pulse repetition interval.
RF	Radio frequency.
RMSE	Root mean square error.
RTT	Round-trip time.
RV-E	Radial velocity estimator.
SAA	Sense and avoid.
SSR	Secondary surveillance radar.
S2V	Sequence to vector.
TCAS	Traffic collision avoidance system.
TO-E	Timing offset estimator.
UAV	Unmanned aerial vehicle.
V2M	Vector to Matrix.
2D	Two-dimensional.
ϕ	Azimuth angle of an aviation obstacle.
θ	Elevation angle of an aviation obstacle.
L	Free space pathloss.
R	Range of the aviation obstacle from the UAV.
T	Half of the PPM symbol time.
T_s	Sampling time.
B	Bandwidth of the received filter.
$\mathbf{f}$	Carrier frequency offset vector (omnidirectional).
$\mathbf{f}^a$	Carrier frequency offset vector (antenna array).
h	Altitude of the UAV measured by its altimeter.
h_a	Altitude of the aviation obstacle.
N	Number of observation samples.
N_a	Number of elements in the planar antenna array.
M_a	Number of scans sweeping the azimuth angle.
M_e	Number of scans sweeping the elevation angle.
τ	Time delay of the DF4 reply at the UAV.
τ_{max}	Maximum time delay for the reception of DF4.
τ_{gr}	Group delay of the receive low-pass filter.
$\mathbf{r}$	DF4 preamble vector of length 16.
$\bar{\mathbf{r}}$	extended preamble vector.
$\mathbf{b}$	DF4 payload vector of length 56.
P_t	Peak transmit power of the DF4 reply.
f_D	Doppler frequency shift.
$z(t)$	Mode S trapezoidal transmit pulse.
$h(t-\tau_{gr})$	low-pass filter at the receiver.
$g(t)$	Received filtered pulse.
$y(t)$	Received baseband signal at the UAV antenna.
$\mathbf{g}$	Vector of length M including the samples of $g(t)$.
v_r	Relative radial velocity.

M	Number of samples per pulse.
$\mathbf{q}$	DF4 preamble and payload vector.
N_0	PSD of noise (W/Hz).
N_{av}	Number of detected aviation obstacles.
$\mathbf{y}$	Received vector by the omnidirectional antenna.
$\mathbf{Y}^{\text{a}}$	Received matrix by the antenna array.
$\mathbf{w}$	AWGN vector of the omnidirectional antenna.
$\mathbf{W}^{\text{a}}$	AWGN matrix of the antenna array.
ϵ_θ	threshold for switching to the RTT-based ranging.
c	Speed of light.
f_{c}	Carrier frequency of the DF4 reply.
λ	Wavelength of the DF4 reply.
$\mathbf{A}$	S correlation matrix in the antenna array.

I. INTRODUCTION

SAA systems enable MAVs and UAVs to integrate safely into civilian airspace by avoiding collisions with other obstacles [1], [2], [3], [4]. An SAA system first monitors the environment surrounding the AV by employing different types of onboard sensors. Following which, it decides whether a collision is impendent and generates a new flight path in order to avoid collision. An advanced SAA system can take advantage of sensor fusion algorithms in combination with image recognition and artificial intelligence to increase the reliability and precision of the system [5]. However, performance improvement is typically achieved at the expense of higher computational complexity and power consumption, which makes on-board processing infeasible for small- and moderate-sized UAVs [6].

Existing SAA solutions for AV can be categorized into noncooperative and cooperative systems. The former SAA systems do not require the cooperation of the obstacles and the AV in the SAA procedure. The sensors used in these SAA systems can be active and/or passive. Active sensors, such as primary radar, ultrasound, and light detection and ranging (LiDAR), emit a signal that is then reflected by an obstacle and detected again by the sensor [7], [8], [9]. Passive sensors detect a signal emitted by the object itself, and include visual and infrared cameras. The later SAA systems are based on the cooperation of the AV and the aviation obstacles (transponder-equipped AVs) within an airspace. The cooperation between the AV and aviation obstacles can be achieved through the SSR Mode A, C, and S transponders [10]. Existing cooperative SAA systems mainly employ the SSR in its Mode S operation. These systems can be categorized as follows:

1) SAA with an onboard interrogator, such as the TCAS, internationally known as the ACAS [11], [12], [13];
2) SAA without an onboard interrogator, for example, the automatic dependent surveillance–broadcast (ADS-B) [14], [15], [16], [17].

Note that the mode S transponders are compatible with Mode A and Mode C SSR.

The ACAS surveillance unit interrogates nearby aviation obstacles, and then, tracks them in the surrounding airspace through replies from their air traffic control transponders. These SAA systems typically obtain the range of each aviation obstacle by measuring the RTT between the transmission of the Mode S interrogation and the receipt of the Mode S downlink reply [18]. The altitude and vertical velocity of each aviation obstacle are determined by tracking the response information of the downlink Mode S [19]. In the SAA systems using ADS-B, the AV and the aviation obstacles are equipped with Mode S transponder and either periodically broadcast and receive identification, position, and other state information without Mode S interrogation. The exchange of position information by the AV and aviation obstacles necessitates the need of the global positioning system in the ADS-B-based SAA systems.

Cooperative SAA offers higher accuracy compared to the noncooperative systems; however, it cannot detect nonaviation obstacles, such as buildings and power lines in urban landscapes. On the contrary, a fast and reliable detection and identification of small-sized UAVs by means of noncooperative SAA systems is challenging. For example, primary radars typically cannot automatically classify whether an object is a bird or an UAV because of the very low radar signatures of the small-sized UAVs (with a radar cross section of the order of 0.01m^2) [20]. The key disadvantage of the noncooperative SAA systems using active ultrasonic sensors or LiDAR is their short-range sensing. Finally, passive sensors, such as visible-light cameras, cannot capture images at night or in low light (at dusk or dawn, in fog, etc.), and detecting small-sized UAVs in infrared images is challenging [21].

Cooperative SAA is significantly effective for detecting and tracking small-sized UAVs. In this regard, a promising solution is to employ and inertial navigation unit in combination with cooperative SAA equipped with an onboard Mode S interrogator and altimeter sensor for altitude measurement.

The radial velocity information of the aviation obstacles can improve the performance of an SAA system. Existing cooperative SAA with an onboard Mode S interrogator, such as the ACAS, can estimate the radial velocity and the vertical velocity of the aviation obstacles by tracking the decoded altitude information. This requires the reception of at least two correctly decoded Mode S downlink replies from each aviation obstacle. Radial velocity estimation using altitude information is accurate for constant relative radial velocity, which is not the case in practice. Furthermore, the standard for Mode S responses allows small timing variances that, although small, affect system performance when used to estimate RTT [11]. Hence, the RTT-based ranging algorithm in the ACAS is not very accurate.

Taking into account the aforementioned limitations and drawbacks of the ACAS, we propose an efficient and low-complexity cooperative SAA system for small-sized UAVs equipped with an onboard Mode S interrogator, inertial navigation unit, and an altimeter. The proposed SAA method can estimate the radial velocity of an aviation obstacle with

a single Mode S downlink reply; hence, it can offer more accurate radial velocity estimation compared to the ACAS. Moreover, it uses the decoded altitude information in the Mode S downlink reply and the estimated elevation angle of the aviation obstacles for ranging. This can improve the accuracy of ranging compared to the RTT-based method used in the ACAS because ranging does not depend on the variances in timing of Mode S reply. Finally, based on sensing information, the proposed SAA method classifies aviation obstacles as low-, medium-, and low-risk intruders. By employing the estimated parameters, the UAV can then decide on the best evasive maneuver or flight path correction to avoid collision.

A. Contributions

Our key contributions are listed as follows.

1) We propose a cooperative SAA method with an onboard mode S interrogator through which a small-size UAV can estimate the radial velocity of the aviation obstacles in the airspace. To do so, we propose a low-complexity and accurate estimator that estimates the Doppler frequency shift from the DF4 reply signal transmitted by the aviation obstacle. We analytically obtain the RMSE of the proposed estimator and the maximum unambiguous radial velocity that can be estimated.
2) The idea of multicarrier transmission for the separation of the Doppler frequency shift and the frequency drift between the oscillators of the aviation obstacle and the UAV in the Mode S operation SSR is proposed.
3) Range measurement by using the triangular relation between the elevation angle of the aviation obstacle and the altitude difference is investigated for mode S operation SSR, and we analytically obtain the RMSE of the ranging method.
4) A low-complexity and efficient intruder identification method for the mode S operation SSR is proposed.

B. Notation

Throughout this article, the superscript T denotes the transpose operator, $*$ is the complex conjugation operator, the symbol $\neg$ is the logical not, $[\cdot]$ and $\otimes$ denote the floor function and the Kronecker product, respectively. The convolution operator is shown by $\circledast$. Vectors and matrices are denoted by bold lowercase and uppercase letters, respectively, and diag($\mathbf{a}$) returns a diagonal matrix with entries of the vector $\mathbf{a}$ along the main diagonal. Vectors $\mathbf{0}_N$ and $\mathbf{1}_N$ denote the all-zero and all-ones vectors of length N, respectively, and the symbol $\hat{x}$ is an estimate of x. The continuous uniform distribution between a and b is denoted by $\mathcal{U}_c(a, b)$. A list of acronyms and the symbols used throughout this article is provided in Nomenclature.

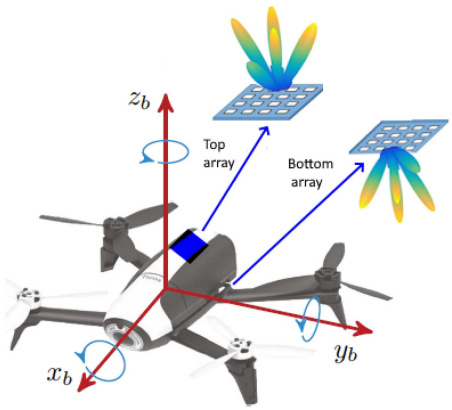

Fig. 1. Body frame (x_b, y_b, z_b) and the 2-D antenna arrays on the $x_b - y_b$ plane for a typical UAV. An omnidirectional antenna is placed close to each antenna array for side-lobe blocking.

C. Outline

The rest of this article is organized as follows. Section II introduces the system model. Section III describes the proposed SAA and the signal model for the SAA system. In Section IV, the radial velocity estimation of the aviation obstacles is discussed. The AOA estimation is studied in Section V. The proposed ranging algorithm and the intruder identification method are investigated in Sections VI and VII, respectively. Simulation results are provided in Section VIII, and finally, Section IX concludes this article.

II. SYSTEM MODEL

We consider that UAVs in the airspace are equipped with a miniaturized Mode S transponder, two onboard omnidirectional antennas, and two planar antenna arrays with $N_a \triangleq N_x \times N_y$ elements, spaced by d_x in the rows and d_y in the columns. Hence, an UAV can electronically perform a beam scan in azimuth and elevation. In practice, two antenna arrays are mounted on the top and bottom of the UAV to be able to scan elevation angles in the range of $(-90, 90)^\circ$ and azimuth angle in the range of $(0, 180)^\circ$. An omnidirectional antenna is also placed close to each antenna array for side-lobe blocking. The UAV switches between the top and bottom antennas according to the direction of its velocity vector. The body frame (x_b, y_b, z_b) and the 2-D antenna array planes of a typical UAV are illustrated in Fig. 1. As seen, the antenna arrays are on the $x_b - y_b$ plane. The onboard antennas enable the transponder to receive the Mode S interrogations at 1030 MHz and reply to them at 1090 MHz.

During navigation, UAVs continuously sense the 1030-MHz radio frequency band using their omnidirectional antenna. For sensing, a simple energy detector can be adopted. As soon as the 1030-MHz channel is identified as unoccupied by a sensing UAV,[1] it initiates the Mode S

[1]We consider a single channel in this article; however, by considering multiple channels, many UAVs can simultaneously initiate Mode S interrogation.

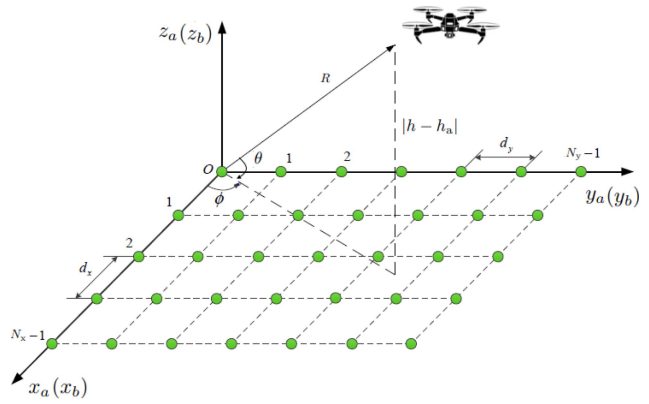

Fig. 2. Azimuth angle ϕ and the elevation angle θ of the target in the body frame (x_b, y_b, z_b) and the top antenna array frame (x_a, y_a, z_a).

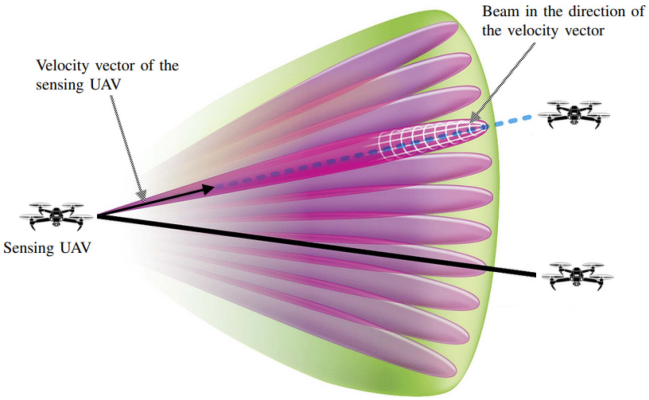

Fig. 3. UAV electronically steers the boresight of the antenna array at its top or bottom in the direction of its velocity vector. To increase the situational awareness, the UAV can sequentially scan an extended angular region.

interrogation by using its antenna array and its omnidirectional antenna [22]. The UAV applies electronic beamforming techniques to the antenna array to scan both azimuth angle, ϕ, and elevation angle, θ, to detect and track the aviation obstacles within the airspace. The azimuth angle, ϕ, and the elevation angle, θ, of the aviation obstacle in the body frame (x_b, y_b, z_b) and the top antenna array frame (x_a, y_a, z_a) are shown in Fig. 2.

The UAV electronically steers the boresight of the antenna array at its top or bottom in the direction of its velocity vector (ϕ_v, θ_v). Moreover, in order to increase the situational awareness, it can sequentially scan an extended angular region in the vicinity of the beam in the direction of its velocity vector as shown in Fig. 3. Within the electronically scanned area, the directional antenna boresight (top and bottom) are located at $(\tilde{\phi}, \tilde{\theta}) \in \mathcal{S}$ with

$$\mathcal{S} = \Big\{ \big(\tilde{\phi} = \phi_v + l\Delta\phi_3, \tilde{\theta} = \theta_v + m\Delta\theta_3\big) \big| l, m \in \mathbb{Z} \\ \tilde{\phi} \in (0, 180), \tilde{\theta} \in (-90, 90) \Big\} \quad (1)$$

where $\mathbb{Z}$ is the set of integers, and $\Delta\phi_3$ and $\Delta\theta_3$ denote the 3-dB beamwidth of the array for the azimuth and elevation angles, respectively.

Let M_a and M_e denote the number of electronic scans sweeping the azimuth and elevation angles, respectively. The frame structure for RF sensing, Mode S uplink interrogations, and downlink responses for M_eM_a beam scans by an UAV are illustrated in Fig. 4. As seen, Mode S interrogation is composed of two phases: 1) UF11 all-call, and 2) UF4 roll-call. In the first phase, the UAV sequentially scans the airspace with M_eM_a beams and transmits the UF11 all-call Mode S interrogation within each beam. During the UF11 all-call interrogation, the sensing UAV obtains the DF11 squitters of all UAVs in its vicinity [22].

In the second phase, after the termination of the UF11 all-call Mode S interrogation for all M_eM_a beams, the UAV sends the UF4 roll-call Mode S interrogation by selectively addressing the detected aviation obstacles. Each aviation obstacle replies to its UF4 roll-call interrogation by broadcasting its altitude information through the DF4 downlink reply from its omnidirectional antenna. In this interrogation-based scheme, a fast moving aviation obstacle can transmit the DF11 reply in one beam, and then, leaves the beam, resulting in it not receiving the UF4 interrogation. This problem can be solved by transmitting the UF4 interrogation in multiple beams regardless of the beamwidth until the UAV receives the DF4 reply of the aviation obstacle .

III. PROPOSED COOPERATIVE SAA METHOD

We consider perfect RF sensing by the UAVs; hence, only a single UAV emits the UF11 all-call, and then, the UF4 roll-call Mode S interrogation signals in each navigation step. We propose a cooperative SAA method that estimates the radial velocity, range, and azimuth and elevation angles of the aviation obstacles from their DF4 roll-call mode S replies. By combining the estimated parameters, the aviation obstacles are classified into high-, medium-, and low-risk intruders for the UAV. The block diagram of the proposed SAA method sensing an aviation obstacle is illustrated in Fig. 5.

The TO-E block is the timing offset estimator and is used to estimate the beginning of the received DF4 Mode S reply of the aviation obstacle, i.e., $\hat{n}_0$. The NC-SD block is the noncoherent symbol detector and is employed to demodulate the DF4 reply packet of the aviation obstacle, i.e., $\hat{\mathbf{b}}$. The proposed RV-E block is the radial velocity estimator and is used to estimate the relative radial velocity of the aviation obstacle, i.e., $\hat{v}_r$. The AoA-E block is the angle-of-arrival estimator and is used to estimate the elevation and azimuth angles of the aviation obstacle, i.e., $\hat{\theta}$ and $\hat{\phi}$, respectively. The decoding block is employed to decode the altitude information of the aviation obstacle, i.e., h_a, from $\hat{\mathbf{b}}$, and the CRC block is used to validate the integrity of the data in $\hat{\mathbf{b}}$. If the CRC verifies the validity of $\hat{\mathbf{b}}$, it is passed through the decoding block to obtain the altitude of the intruder. The elevation angle and the altitude of the aviation obstacle are employed to estimate range $\hat{R}$. If the CRC does not verify the validity of $\hat{\mathbf{b}}$ or $|\hat{\theta}| < \epsilon_\theta$, the RTT-based ranging is employed. The outputs of the parameter estimators, i.e., $\hat{v}_r$,

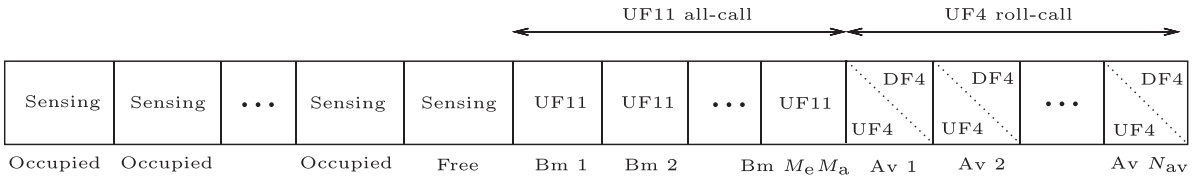

Fig. 4. Frame structure for RF sensing, the UF11 all-call, and roll-call UF4 Mode S interrogations for $M_e M_a$ beam scans by the UAV. After the reception of the UF4 by the aviation obstacle, it sends the DF4 reply. Bm and Av stand for beam and aviation obstacle, respectively. The total number of aviation obstacles detected by the UAV during the UF11 all-call is denoted by N_{av}.

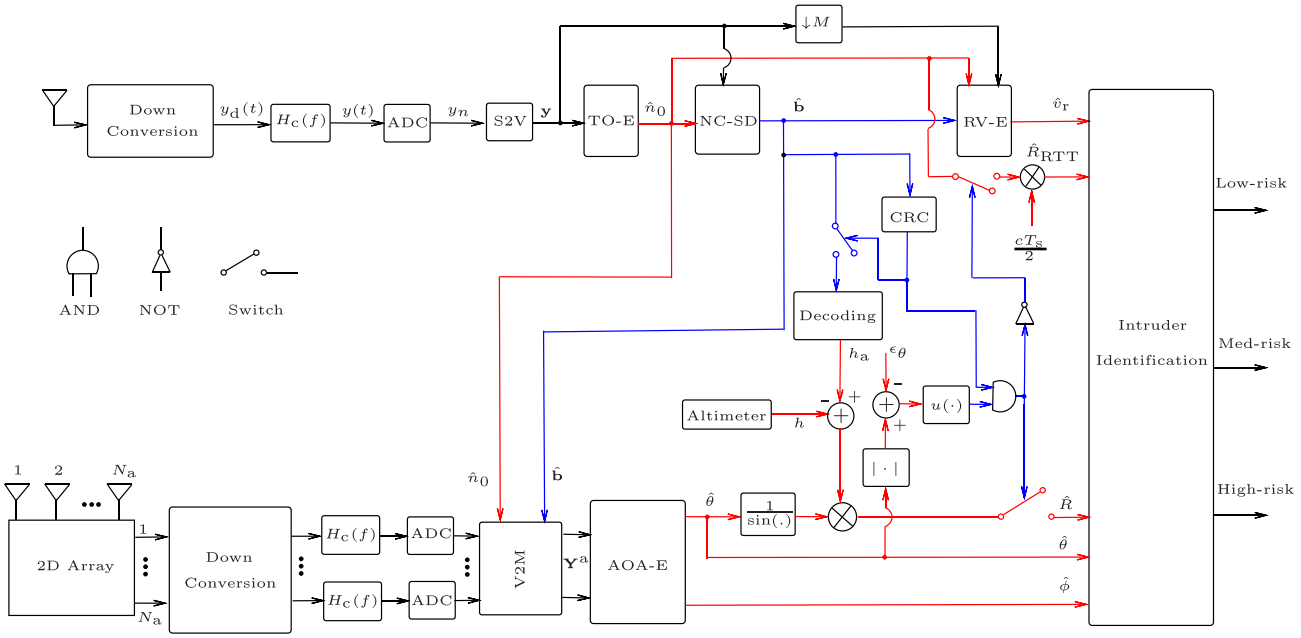

Fig. 5. Block diagram of the proposed SAA system sensing an aviation obstacle using its top/bottom antenna array and its top/bottom omnidirectional antenna. The number of antenna elements of the array is $N_a = N_x N_y$, $\downarrow M$ denotes the M-fold decimation, $u(\cdot)$ is the unit step function with $u(x) = 1$, for $x \geq 0$, and $u(x) = 0$, for $x < 0$, and ϵ_θ is a threshold used to switch between the proposed ranging algorithm and the RTT-based ranging. The abbreviations are: analog-to-digital converter (ADC), sequence to vector (S2V, vector to matrix (V2M), timing offset estimator (TO-E), noncoherent symbol detector (NC-SD), radial velocity estimator (RV-E), cyclic redundancy check (CRC), and angle-of-arrival estimator (AOA-E). The black, red, and blue solid lines show the raw data, real values, and logical values, respectively.

$\hat{R}$, $\hat{\theta}$, and $\hat{\phi}$ are used as inputs of the intruder identification unit. In the following, the aforementioned blocks and the intruder identification unit are studied in details.

A. Mode S DF4 Discrete Time Signal Model

Let us consider that the DF4 packet of an aviation obstacle is received at the UAV's omnidirectional antenna with a time delay of $\tau \in (0, \tau_{\max}]$ in the receiver time reference, where τ is unknown, and $\tau_{\max}$ is known and denotes the maximum delay between the transmission of the UF4 Mode S interrogation signal by the UAV and the reception of the DF4 reply from an aviation obstacle.

As shown in Fig. 5, the downconverted DF4 reply signal at the UAV's omnidirectional antenna, i.e., $y_d(t)$, is passed through the low-pass filter with frequency response $H_c(f) = |H(f)| \exp(j(\angle H(f) - 2\pi f \tau_{gr}))$, $f \in [-B, B]$, where B is the bandwidth of the low-pass filter. The impulse response of the filter is $h(t - \tau_{gr})$, where $\tau_{gr} - \frac{1}{2\pi} \frac{d\angle H(f)}{df}$ is the group delay of the filter and $h(t) \triangleq \mathcal{F}^{-1}\{|H(f)| \exp(j\angle H(f))\}$ with $\mathcal{F}^{-1}$ as the inverse Fourier transform. Without loss of generality, we assume that $E_h = \int_{-\infty}^{+\infty} h^2(t)dt = \int_{-B}^{+B} |H(f)|^2 df = 1$. The complex baseband filtered signal $y(t)$ can be written as[2] [23]

$$y(t) = \frac{\sqrt{P_t \eta_0}}{L}\Bigg[\sum_{m=0}^{15} r_m g\Big(t - mT - \frac{T}{2} - \tau_{gr} - \tau\Big) + \sum_{m=9}^{64} g\Big(t - 2mT + b_{(m-9)}T + \frac{T}{2} - \tau_{gr} - \tau\Big)\Bigg] e^{j(2\pi f_D t + \psi_0)} + w(t), \qquad 0 \leq t \leq 128T + \tau_{gr} + \tau_{\max}. \tag{2}$$

The first term in (2) denotes the waveform of the DF4 reply associated with the preamble, and the second term denotes the waveform associated with the PPM signaling.

[2]We include the filtering and sampling procedures to emphasize that ideal PPM waveform cannot be considered in the analysis of the DF4 reply signal at the receiver.

For Mode S [22]

$$\mathbf{r} = [r_0\ r_1\ \ldots\ r_{15}]^{\mathrm{T}} \triangleq \left[1\,0\,1\,0\,0\,0\,0\,1\,0\,1\,0\,0\,0\,0\,0\,0\right]^{\mathrm{T}} \tag{3}$$

which denotes the preamble vector, and

$$\mathbf{b} = [b_0\ b_1\ \ldots\ b_{55}]^{T} \tag{4}$$

contains the surveillance, communication, and control data along with the parity bits, called payload bits. In (2), P_{t}, η_0, $2T = 1\mu$s, f_{D}, and ψ_0 denote the peak transmit power, the radiation efficiency of the omnidirectional antenna, the signaling time of the PPM, the Doppler frequency shift, and the carrier phase offset, respectively. Moreover, L denotes the free space pathloss between the aviation obstacle and the UAV defined as $L \triangleq \frac{4\pi R}{\lambda}$, where λ and R denote the carrier wavelength and the distance between the aviation obstacle and the UAV, respectively. The pulse $g(t)$ in (2) is given by $g(t) \triangleq z(t) \circledast h(t)$, where $z(t)$ is the Mode S trapezoidal transmit pulse defined as [23]

$$z(t) = \begin{cases} \frac{A\left(t+\frac{T}{2}\right)}{\tau_{\mathrm{r}}} & -\frac{T}{2} \le t < -\frac{T}{2}+\tau_{\mathrm{r}} \\ A & -\frac{T}{2}+\tau_{\mathrm{r}} \le t \le \frac{T}{2}-\tau_{\mathrm{r}} \\ \frac{A\left(-t+\frac{T}{2}\right)}{\tau_{\mathrm{r}}} & \frac{T}{2}-\tau_{\mathrm{r}}, < t \le \frac{T}{2} \end{cases} \tag{5}$$

where the rise and decay time of the pulse $z(t)$ is τ_{r}, and A is a constant value that satisfies $P_{\mathrm{z}} = \frac{1}{T}\int_{-\frac{T}{2}}^{\frac{T}{2}} z^2(t)\mathrm{d}t = 1$. The average received power at the receiver is given by $P_{\mathrm{av}} \approx \frac{P_{\mathrm{t}}\eta_0}{2L^2T}\int_{-T/2}^{T/2} g^2(t)\mathrm{d}t$, and the power spectral density (PSD) of the additive noise $w(t)$ is N_0 W/Hz over the low-pass filter bandwidth, i.e., $f \in [-B, B]$. In cooperative and RF-based sense and avoid systems, moderately high signal-to-noise (SNR) is required to achieve low bit error rate, and thus, reliable noncoherent DF4 packet decoding [24].

The received signal in (2) is sampled with sampling rate $R_{\mathrm{s}} = 1/T_{\mathrm{s}}$, where T_{s} is the sampling time. The discrete received baseband signal for the omnidirectional antenna can be written as

$$\mathbf{y} \approx \frac{\sqrt{P_{\mathrm{t}}\eta_0}}{L}\mathbf{F}\mathbf{s} + \mathbf{w} \tag{6}$$

where $\mathbf{F} \triangleq \mathrm{diag}(\mathbf{f})$

$$\mathbf{f} \triangleq \left[e^{j\psi_0}\ e^{j(2\pi f_{\mathrm{D}}T_{\mathrm{s}}+\psi_0)}\ \ldots\ e^{j(2\pi f_{\mathrm{D}}T_{\mathrm{s}}(N-1)+\psi_0)}\right]^{\mathrm{T}} \tag{7a}$$

$$\mathbf{y} \triangleq \left[y_0\ y_1\ \ldots\ y_{N-1}\right]^{\mathrm{T}} \tag{7b}$$

$$\mathbf{s} \triangleq \left[\mathbf{0}_d^{\mathrm{T}}\ (\mathbf{q}\otimes\mathbf{g})^{\mathrm{T}}\ \mathbf{0}_{D-d}^{\mathrm{T}}\right]^{\mathrm{T}} \tag{7c}$$

$$\mathbf{q} \triangleq \left[\mathbf{r}^{\mathrm{T}}\ b_0\ \neg b_0\ b_1\ \neg b_1\ \ldots\ b_{55}\ \neg b_{55}\right]^{\mathrm{T}} \tag{7d}$$

$$\mathbf{g} \triangleq \left[g_0\ g_1\ \ldots\ g_{M-1}\right]^{\mathrm{T}} \tag{7e}$$

$$\mathbf{w} \triangleq \left[w_0\ w_1\ \ldots\ w_{N-1}\right]^{\mathrm{T}} \tag{7f}$$

$y_k \triangleq y(kT_{\mathrm{s}})$, $w_k \triangleq w(kT_{\mathrm{s}})$, $k = 0, 1, \ldots, N-1$, $g_m \triangleq g(mT_{\mathrm{s}} - \frac{T}{2})$, $m = 0, 1, \ldots, M-1$, and $N \triangleq 128M + D$ with

$$M \triangleq \left\lfloor \frac{T}{T_{\mathrm{s}}} \right\rfloor,\quad D = \left\lfloor \frac{\tau_{\max}+\tau_{\mathrm{gr}}}{T_{\mathrm{s}}} \right\rfloor + 1,\quad d = \left\lfloor \frac{\tau+\tau_{\mathrm{gr}}}{T_{\mathrm{s}}} \right\rfloor + 1 \tag{8}$$

where $2M$ is the number of samples per PPM symbol time, $2T$. For the practical square-root raised cosine low-pass filter $H(f)$ with bandwidth B and roll-off factor β, the sampling rate $R_{\mathrm{s}} = 2B/(1+\beta)$ results in independent and identically distributed additive noise at the receiver. In this case, the noise vector $\mathbf{w}$ in (6) is zero-mean AWGN with variance $\sigma_{\mathrm{w}}^2 = N_0E_{\mathrm{h}} = N_0$, where $E_{\mathrm{h}} = 1$ is the energy of the low-pass filter $h(t)$. The values of ψ_0 and f_{D} are unknown at the receiver.

B. TO-E and NC-SD Blocks

In this subsection, we briefly study the TO-E and NC-SD blocks because their outputs are used in the proposed RV-E and the ranging algorithm as shown in Fig. 5.

1) *Timing Offset Estimator (TO-E):* For exclusive SAA applications, because the response of the aviation obstacle to the UF4 roll-call Mode S interrogation is DF4 reply and this is known to the UAV, the preamble vector in (3) along with the five PPM symbols denoting the format number of the packet can be employed for time synchronization. Thus, the preamble vector used for time synchronization can be extended to

$$\bar{\mathbf{r}} \triangleq \left[\bar{r}_0\ \bar{r}_1\ \ldots\ \bar{r}_{25}\right]^{\mathrm{T}} = \left[\mathbf{r}^{\mathrm{T}}\ 0\,1\,0\,1\,1\,0\,0\,1\,0\,1\right]^{\mathrm{T}} \tag{9}$$

where $\mathbf{r}$ is given in (3). By employing the correlation estimator, the beginning of the DF4 packet n_0 can be straightforwardly estimated as [22]

$$\hat{n}_0 = \underset{n_0}{\mathrm{argmax}} \left| \sum_{n=n_0}^{n_0+25} y_n^* \bar{r}_{n-n_0} \right|^2 \quad \text{s.t.} \quad M_{\mathrm{gr}} \le n_0 \le D \tag{10}$$

where $M_{\mathrm{gr}} \triangleq \lfloor \frac{\tau_{\mathrm{gr}}}{T_{\mathrm{s}}} \rfloor + 1$.

2) *Noncoherent Symbol Detector (NC-SD):* After estimating the beginning of the DF4 response packet, the PPM data symbols can be noncoherently detected as

$$\hat{b}_n = \begin{cases} 1 & \text{if } \sum_{m=0}^{M-1}\Lambda_{n,m} \ge \sum_{m=M}^{2M-1}\Lambda_{n,m} \\ 0 & \text{if } \sum_{m=0}^{M-1}\Lambda_{n,m} < \sum_{m=M}^{2M-1}\Lambda_{n,m} \end{cases} \tag{11}$$

for $n = 0, 1, \ldots, 55$, where $\hat{b}_n$ is the nth decoded data bit, and $\Lambda_{n,m} \triangleq \left|y_{\hat{n}_{\mathrm{s}}+2nM+m}\right|^2$, $\hat{n}_{\mathrm{s}} \triangleq \hat{n}_0 + 16M$. By decoding the detected bits $\hat{b}_n$ in (11), the altitude of the aviation obstacle is obtained. The altitude information can be used for radial velocity estimation and ranging.

IV. PROPOSED RV-E

It this section, we investigate in detail the RV-E block in Fig. 5 and demonstrate how the detected DF4 reply can be employed for radial velocity estimation of the aviation obstacles. The proposed RV-E is one of the main contributions of this article.

The Doppler frequency shift f_{D} in (2) can be expressed as a function of the relative radial velocity of the aviation obstacle and UAV, v_{r}, as

$$f_{\mathrm{D}} = \frac{v_{\mathrm{r}}f_{\mathrm{c}}}{c} \tag{12}$$

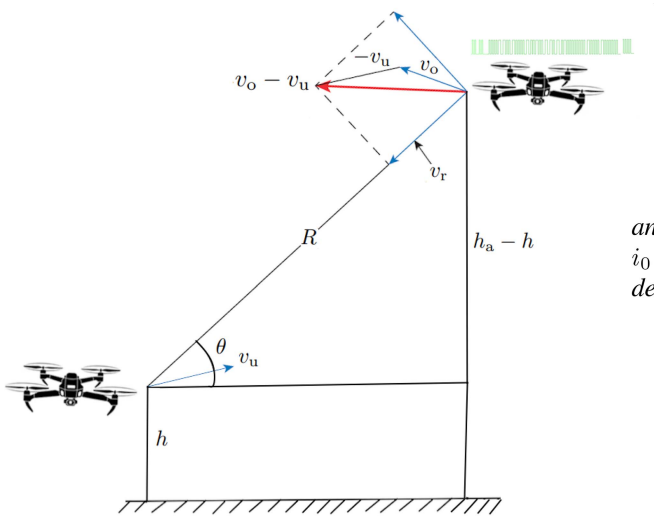

Fig. 6. Velocity vector of the UAV, v_u, the velocity vector of the aviation obstacle, v_o, the relative velocity vector $v_o - v_u$, the radial velocity vector v_r, the altitude of the UAV, h, and the altitude of the aviation obstacle, h_a.

where $c = 3 \times 10^8$ m/s and $f_c = 1090 \times 10^6$ Hz denote the speed of light and the carrier frequency of the DF4 reply, respectively. The relative radial velocity of the UAV and an aviation obstacle is shown in Fig. 6. For the derivation of the RV-E, we consider perfect time delay estimation, i.e., $\hat{n}_0 = n_0$, and perfect data detection, i.e., $\hat{\mathbf{b}} = \mathbf{b}$. However, in practice, the estimated time delay and the detected PPM data are replaced in the derived RV-E.

Let n_0 denote the index of the first sample of the received DF4 reply. The index of the sample denoting the start of the payload symbols is $n_s \triangleq n_0 + 16M$ because the length of the sampled preamble vector in (3) is $16M$. Let us write the PPM form of the payload vector $\mathbf{b}$ in (4) as

$$\begin{aligned}\bar{\mathbf{b}} &= \left[\bar{b}_0\ \bar{b}_1\ \ldots\ \bar{b}_{111}\right]^{\mathrm{T}} \\ &\triangleq \left[b_0\ \neg b_0\ b_1\ \neg b_1\ \ldots\ b_{55}\ \neg b_{55}\right]^{\mathrm{T}}\end{aligned} \tag{13}$$

and let $\mathcal{I}$ denote the set that includes the index of the nonzero elements of the vector $\bar{\mathbf{b}}$, defined as

$$\mathcal{I} = \{i_0, i_1, \ldots, i_{55}\} \triangleq \{i \in \{0, 1, \ldots, 111\} | \bar{b}_i \neq 0\}. \tag{14}$$

The cardinality of $\mathcal{I}$ is $|\mathcal{I}| = 56$ because of the PPM signaling of $\bar{\mathbf{b}}$. In Theorem 1, we propose a low-complexity and accurate Doppler frequency shift estimator using the DF4 reply of an aviation obstacle.

THEOREM 1 At moderately high SNR values that is the case in cooperative and RF-based SAA systems, the Doppler frequency shift f_D between the UAV and an aviation obstacle can be estimated by

$$\hat{f}_D = \frac{\hat{v}_r f_c}{c} = \frac{1}{2\pi M T_s} \frac{\mathbf{u}^{\mathrm{T}} \boldsymbol{\Delta}^{\mathrm{T}} \mathbf{C}^{-1} \boldsymbol{\Delta} \boldsymbol{\varphi}}{\mathbf{u}^{\mathrm{T}} \boldsymbol{\Delta}^{\mathrm{T}} \mathbf{C}^{-1} \boldsymbol{\Delta} \mathbf{u}} \tag{15}$$

where

$$\boldsymbol{u} \triangleq \left[i_0\ i_1\ \ldots\ i_{55}\right]^{\mathrm{T}} \tag{16a}$$

$$\boldsymbol{\varphi} \triangleq \left[\angle x_{i_0}\ \angle x_{i_1}\ \ldots\ \angle x_{i_{55}}\right]^{\mathrm{T}} \tag{16b}$$

$$x_i \triangleq y_{n_d + iM} \tag{16c}$$

$$n_d \triangleq n_0 + 16M + [M/2] \tag{16d}$$

and the elements of the vector $\boldsymbol{u}$, are given in (14) with $i_0 < i_1 < \ldots < i_{55}$. In (15), $\boldsymbol{\Delta}$ is the 55×56 discrete derivative matrix as

$$\boldsymbol{\Delta} \triangleq \begin{bmatrix} 1 & -1 & 0 & 0 & 0 & \cdots & 0 \\ 0 & 1 & -1 & 0 & 0 & \cdots & 0 \\ \vdots & \ddots & \ddots & \ddots & \ddots & \cdots & \vdots \\ 0 & 0 & \cdots & 1 & -1 & 0 & 0 \\ 0 & 0 & \cdots & 0 & 1 & -1 & 0 \\ 0 & 0 & \cdots & 0 & 0 & 1 & -1 \end{bmatrix} \tag{17}$$

and $\mathbf{C}$ is the 55×55 square matrix as

$$\mathbf{C} = \sigma_\vartheta^2 \begin{bmatrix} 2 & -1 & 0 & 0 & \cdots & 0 \\ -1 & 2 & -1 & 0 & \cdots & 0 \\ \cdots & \cdots & \cdots & \cdots & \cdots & \cdots \\ 0 & 0 & \cdots & 0 & -1 & 2 \end{bmatrix} \tag{18}$$

with

$$\sigma_\vartheta^2 \triangleq \frac{1}{2}\left(\frac{L\sigma_w}{\sqrt{P_t \eta_0 g_{n_c}}}\right)^2 \tag{19}$$

and g_{n_c} with $n_c \triangleq [M/2]$, is the $(n_c + 1)$th elements of the pulse shaping vector $\mathbf{g}$ given in (7e).

The Doppler frequency shift estimator in (15) is an unbiased estimator, i.e., $\mathbb{E}\{\hat{f}_D\} = f_D$, and its RMSE is given by

$$\sqrt{\mathbb{E}\{(f_D - \hat{f}_D)^2\}} = \sqrt{\frac{1}{(2\pi M T_s)^2} \frac{1}{\mathbf{u}^{\mathrm{T}} \boldsymbol{\Delta}^{\mathrm{T}} \mathbf{C}^{-1} \boldsymbol{\Delta} \mathbf{u}}}. \tag{20}$$

■

Proof is in Appendix A.

Note that the inverse of the matrix $\mathbf{C}$ is given by $[\mathbf{C}^{-1}]_{mn} = \sigma_\vartheta^{-2}\left[\min(m, n) - \frac{mn}{56}\right]$, where $1 \leq m, n \leq 55$ and $\min(m, n)$ denotes the minimum of m and n [25]. As seen, the estimator in (15) does not require a priori knowledge on σ_ϑ^2, and thus, the path loss L and the transmit power P_t.

PROPOSITION 1 Maximum Unambiguous Radial Velocity

PPM signaling can be considered a waveform of pulse radar with random PRIs of length T, $2T$, and $3T$, and pulsewidth T. Hence, the maximum unambiguous Doppler frequency shift that can be estimated is given by

$$|f_D| \leq \frac{1}{T} \tag{21}$$

which results in the maximum relative radial velocity of

$$|v_r| \leq \frac{\lambda}{T}. \tag{22}$$

Proof is in Appendix B.

PROPOSITION 2 Separation of the Doppler Frequency Shift and the Frequency Drift.

In addition to Doppler frequency shift due to the relative radial velocity between the UAV and the aviation obstacle, there is always some difference between the manufacturer's nominal operational frequency and the real frequency of the Mode S transponder. Moreover, the actual frequency keeps slightly changing with temperature, pressure, age, and some other factors. Hence, a frequency drift between the UAV and the aviation obstacle oscillators is expected.

Distinguishing between frequency drift and Doppler frequency shift is impossible for a single-carrier communication, as is currently in Mode S SSR. However, frequency drift and Doppler frequency shift can be separated in multicarrier communication with at least two subcarriers. Hence, for applications requiring high precision radial velocity estimation, the DF4 replies need to be transmitted in the form of multicarrier.

Let df denote the frequency drift between the transmitter and receiver oscillators of a multicarrier system with subcarrier frequencies $Q_k\Delta f$, $k \in \{0, 1, \ldots, N_c - 1\}$ in the baseband, where Δf and N_c, denote the subcarrier bandwidth and the number of subcarriers, respectively. Because of the frequency drift, the frequency offset of the kth subcarrier f_k can be written as

$$f_k \approx \frac{v_r(f_c + Q_k\Delta f)}{c} + df \tag{23}$$

where $k = 0, 1, \ldots, N_c - 1$, f_c is the carrier frequency, and c denotes the speed of light.

Let $\hat{f}_k$ denote the estimation of f_k by using the proposed estimator in (15). We can write $\boldsymbol{\Omega} \triangleq [\hat{f}_0\ \hat{f}_1\ \ldots\ \hat{f}_{N_c-1}]^T$ in vector form as

$$\boldsymbol{\Omega} = \boldsymbol{\Psi}\boldsymbol{\eta} + \mathbf{z} \tag{24}$$

where $\mathbf{z}$ is the additive noise vector, $\boldsymbol{\eta} \triangleq [df\ v_r]^T$, and

$$\boldsymbol{\Psi} \triangleq \begin{bmatrix} 1 & \frac{f_c+Q_0\Delta f}{c} \\ 1 & \frac{f_c+Q_1\Delta f}{c} \\ \vdots & \vdots \\ 1 & \frac{f_c+Q_{N_c-1}\Delta f}{c} \end{bmatrix}. \tag{25}$$

The LS estimate of $\boldsymbol{\eta}$ is expressed as

$$\hat{\boldsymbol{\eta}} = \underset{\boldsymbol{\eta}}{\text{argmax}} \quad \left\|\boldsymbol{\Omega} - \boldsymbol{\Psi}\boldsymbol{\eta}\right\|^2 \tag{26}$$

which yields $\hat{\boldsymbol{\eta}} = [\hat{df}\ \hat{v}_r]^T = (\boldsymbol{\Psi}^T\boldsymbol{\Psi})^{-1}\boldsymbol{\Psi}^T\boldsymbol{\Omega}$. It is obvious that the Doppler frequency shift of the kth subcarrier is estimated as $\hat{v}_r(f_c + Q_k\Delta f)/c$.

V. AOA ESTIMATION

In this section, we investigate the AOA-E block in Fig. 5. The estimated elevation angle of the aviation obstacle θ is used in the proposed ranging algorithm in Section VI. To estimate the azimuth and elevation angles of aviation obstacles, the SAA system uses its 2-D planar antenna array. For AOA estimation, we use the 56 M received samples corresponding to the elements of $\bar{\mathbf{b}}$ in (13) with the indices in the set $\mathcal{I}$ in (14). In this case, the received discrete baseband matrix in the antenna array with $N_a \triangleq N_xN_y$ antenna elements can be written as

$$\begin{aligned}\mathbf{Y}^a &= \left[\mathbf{y}_1^a\ \mathbf{y}_2^a\ \ldots \mathbf{y}_{N_a}^a\right] \\ &\approx \frac{\alpha f(\theta,\phi)\sqrt{P_t\eta}}{L}\mathbf{F}^a(\mathbf{1}_{56}\otimes\mathbf{g})\mathbf{a}^T(\theta,\phi) + \mathbf{Z}^a\end{aligned} \tag{27}$$

where $\mathbf{Y}^a$ is the $56M \times N_a$ measurement matrix, $f(\theta, \phi)$ is the normalized field pattern[3] (normalized to unity), α is a nominal field amplitude by the aviation obstacle, P_t is the peak transmit power by the aviation obstacle, η is the radiation efficiency of the array, $\mathbf{F}^a \triangleq \text{diag}(\mathbf{f}^a)$ with

$$\mathbf{f}^a \triangleq \left[\mathbf{f}_{i_0}^T\ \mathbf{f}_{i_1}^T \ldots\ \mathbf{f}_{i_{55}}^T\right]^T \tag{28}$$

$$\mathbf{f}_i \triangleq \left[e^{j(2\pi f_D T_s(n_s+iM)+\psi_a)}\ e^{j(2\pi f_D T_s(n_s+iM+1)+\psi_a)} \ldots e^{j(2\pi f_D T_s(n_s+(i+1)M-1)+\psi_a)}\right]^T \tag{29}$$

$n_s = n_0 + 16M$, $i_k \in \mathcal{I}$, the carrier phase offset of the array is ψ_a,[4] and $\mathbf{1}_{56}$ denotes all-ones vector of length 56. The array manifold vector of the 2-D planar antenna array with $N_x \times N_y$ elements, spaced by d_x in the rows and d_y in the columns is $\mathbf{a}(\theta, \phi) \triangleq [a_{1,1}(\theta, \phi), a_{2,1}(\theta, \phi), \ldots, a_{N_x,N_y}(\theta, \phi)]^T$ [26], where

$$a_{m,n}(\theta,\phi) = e^{j\frac{2\pi}{\lambda}(d_x(m-1)\cos(\theta)+d_y(n-1)\sin(\theta)\sin(\phi))}. \tag{30}$$

The complex-valued AWGN matrix $\mathbf{Z}^a$ with dimension $56M \times N_a$ in (27) is given by $\mathbf{Z}^a \triangleq \left[\mathbf{z}_1^a\ \mathbf{z}_2^a\ \ldots\ \mathbf{z}_{N_a}^a\right]$, where $\mathbb{E}\left\{\mathbf{z}_k^a(\mathbf{z}_\ell^a)^H\right\} = \delta[k-\ell]\sigma_w^2\mathbf{I}_{56M}, k, \ell \in \{1, 2, \ldots, N_a\}$, and $\sigma_w^2 = N_0E_h = N_0$.

A. 2D-Multiple Signal Classification (2D-MUSIC) Algorithm

To estimate θ and ϕ, different algorithms can be employed. If P_t or R are unknown, the 2D-MUSIC algorithm is an effective method for estimating AOA. By employing the 2D-MUSIC algorithm, the elevation and azimuth angles of the aviation obstacle can be estimated from its DF4 reply as

$$\begin{aligned}\{\hat{\theta}, \hat{\phi}\} = \text{argmax} \quad & P_{2D-MUSIC}(\theta,\phi), \\ \text{s.t.} \quad & \theta \in [\theta_l^{11}, \theta_u^{11}] \\ & \phi \in [\phi_l^{11}, \phi_u^{11}]\end{aligned} \tag{31}$$

where

$$P_{2D-MUSIC}(\theta,\phi) \triangleq \frac{1}{\sum_{n=2}^{N_a}\left|\mathbf{a}^H(\theta,\phi)\hat{\mathbf{e}}_n\right|^2}. \tag{32}$$

The constraint of the maximization in (31), i.e., $\phi \in [\phi_l^{11}, \phi_u^{11}]$ and $\theta \in [\theta_l^{11}, \theta_u^{11}]$, is the angular scanning area, in which the UAV sends the all-call UF11 Mode S interrogation signal to the aviation obstacles, and $\hat{\mathbf{e}}_n$ is the eigenvector corresponding to the nth largest eigenvalue of the sample

[3]For antenna array with omnidirection elements, we have $f(\theta, \phi) = 1$.

[4]Because a single RF oscillator is employed at the antenna array, the carrier phase ψ_a is the same for all array elements.

correlation matrix given by $\hat{\mathbf{A}} = \frac{1}{56M}(\mathbf{Y}^{\mathrm{a}})^{\mathrm{H}}\mathbf{Y}^{\mathrm{a}}$, where $\mathbf{Y}^{\mathrm{a}}$ is the matrix of received samples given in (27). In Appendix C, the performance analysis of the 2-D-MUSIC algorithm for the DF4 reply is provided.

VI. PROPOSED RANGING ALGORITHM BASED ON TRIANGULAR RELATION

In this section, we develop a ranging algorithm using the triangular relation between the elevation angle θ of the aviation obstacle and its altitude difference with the UAV, $h_{\mathrm{a}} - h$. The proposed ranging algorithm is one of the main contributions of this article. By employing $\hat{\theta}$ via either the top or the bottom antennas and the altitude information of the aviation obstacle, i.e., h_{a}, obtained by DF4 reply decoding, the UAV can estimate the range of the aviation obstacle as

$$\hat{R} = \frac{h_{\mathrm{a}} - h}{\sin(\hat{\theta})} \tag{33}$$

where h is the altitude of the UAV measured by its altimeter. The necessary condition for ranging on the basis of triangular relation in (33) is that the CRC is satisfied and $|\hat{\theta}| > \epsilon_\theta$, where ϵ_θ is a predefined threshold. Otherwise, the SAA system can employ the conventional RTT-based ranging algorithm as shown in Fig. 5. It should be noted that for the top (bottom) antenna array, we have $\hat{\theta} > 0$ ($\hat{\theta} < 0$). In Theorem 2, we obtain approximate expressions for the mean and RMSE of the range estimator in (33).

THEOREM 2 : At moderately high SNR values that is the case in cooperative and RF-based SAA systems, the mean and RMSE of the range estimator in (33) for $\theta \in (-90, 90)$ and $\theta \neq 0$ is given by

$$\mathbb{E}\{\hat{R}\} = \mathbb{E}\left\{\frac{h_{\mathrm{a}} - h}{\sin(\hat{\theta})}\right\} \approx \frac{h_{\mathrm{a}} - h}{\sin(\theta)} \tag{34}$$

and

$$\sqrt{\mathbb{E}\{(\hat{R} - R)^2\}} \approx \frac{|h_{\mathrm{a}} - h|}{\sin^2(\theta)} \times \sqrt{\frac{\frac{\sigma_{\mathrm{w}}^2}{112M}\frac{\lambda_{\max}}{(\sigma_{\mathrm{w}}^2 - \lambda_{\max})^2}\left|\mathbf{a}^{\mathrm{H}}(\theta,\phi)\mathbf{e}_1\right|^2}{\sum_{n=2}^{N_{\mathrm{a}}}\left|\boldsymbol{\alpha}^{\mathrm{H}}(\theta,\phi)\mathbf{e}_n\right|^2}} \tag{35}$$

where $\boldsymbol{\alpha}(\theta,\phi) \triangleq \left[\alpha_{1,1}(\theta,\phi)\ \alpha_{2,1}(\theta,\phi)\ \ldots\ \alpha_{N_{\mathrm{x}},N_{\mathrm{y}}}(\theta,\phi)\right]^{\mathrm{T}}$ with $\alpha_{m,n}(\theta,\phi)$ as

$$\alpha_{m,n}(\theta,\phi) \triangleq \frac{\partial a_{m,n}(\theta,\phi)}{\partial \sin(\theta)} = \frac{j2\pi}{\lambda}\Big(d_{\mathrm{y}}(n-1)\sin(\phi) - \tan(\theta)d_{\mathrm{x}}(m-1)\Big)a_{m,n}(\theta,\phi) \tag{36}$$

and $a_{m,n}(\theta,\phi)$ is given in (30). In (35), the vector $\mathbf{e}_1$ is the eigenvector corresponding to the largest eigenvalue of $\boldsymbol{\Lambda} \triangleq \xi\mathbf{a}^*(\theta,\phi)\mathbf{a}^{\mathrm{T}}(\theta,\phi) + \sigma_{\mathrm{w}}^2\mathbf{I}$, i.e., $\lambda_{\max}$, $\mathbf{e}_k$, $k = 2, 3, \ldots, N_{\mathrm{x}}N_{\mathrm{y}}$ are the eigenvectors corresponding to the $N_{\mathrm{x}}N_{\mathrm{y}} - 1$ eigenvalues $\lambda = \sigma_{\mathrm{w}}^2$, and

$$\xi \triangleq \frac{\alpha^2 f^2(\theta,\phi)P_{\mathrm{t}}\eta\sum_{k=1}^{M} g_k^2}{L^2M} \approx \frac{\alpha^2 f^2(\theta,\phi)P_{\mathrm{t}}\eta\int_{-\infty}^{\infty} g^2(t)\mathrm{d}t}{TL^2}. \tag{37}$$

The approximation in (37) is obtained for large enough M, where $\frac{1}{M}\sum_{k=1}^{M} g_k^2 \approx \frac{1}{T}\int_{-\infty}^{\infty} g^2(t)\mathrm{d}t$.

■

Proof is in Appendix D.

VII. INTRUDER IDENTIFICATION

Let ϕ_{v} and θ_{v} denote the direction of the UAV velocity vector in the antenna array coordinate. By estimating $\hat{v}_{\mathrm{r}}$, $\hat{\phi}$, $\hat{\theta}$, and $\hat{R}$ through (15), (31), and (33), the UAV obtains the necessary information for classification of the aviation obstacles. The typical criteria used to evaluate the risk of a collision depend on the class of UAVs. In this article, we propose an intruder identification mechanism in which the UAV uses $\hat{v}_{\mathrm{r}}$, $\hat{\phi}$, $\hat{\theta}$, and $\hat{R}$ to classify aviation obstacles into three classes: 1) high-risk intruder H_0; 2) medium-risk intruder H_1; and 3) and low-risk intruder H_2. We assume that the angular velocities of the aviation obstacle in the antenna array coordinate, i.e., $|\mathrm{d}\phi/\mathrm{d}t|$ and $|\mathrm{d}\theta/\mathrm{d}t|$ are small.

In SAA systems, a safety radius λ_R is considered for safe navigation, and if the distance between the UAV and the aviation obstacle is smaller than this safety radius, the risk of collision is significantly high regardless of radial velocity v_{r}, the relative azimuth angle $|\phi - \phi_{\mathrm{v}}|$, and relative elevation angle $|\theta - \theta_{\mathrm{v}}|$ [27]. The aviation obstacle within the safety radius is identified as a high-risk intruder. Furthermore, in the case that the aviation obstacle is outside the safety radius, the radial velocity, v_{r}, exceeds a safety threshold γ_{v}, and the UAV and the aviation obstacle are moving toward each other, i.e., ($|\phi - \phi_{\mathrm{v}}| < \gamma_\phi$) and ($|\theta - \theta_{\mathrm{v}}| < \gamma_\theta$), the aviation obstacle is also identified as a high-risk intrusion because the risk of collision is still high.

In the case that the radial velocity, v_{r}, exceeds the safety threshold, γ_{v}, and the UAV and aviation obstacle are not moving toward each other, i.e., ($|\phi - \phi_{\mathrm{v}}| > \gamma_\phi$) or ($|\theta - \theta_{\mathrm{v}}| > \gamma_\theta$), the aviation obstacle is identified as a medium-risk intruder because it has the potential to rapidly reach the safety radius. Finally, in the case that the aviation obstacle is outside the safety radius, and the radial velocity, v_{r}, does not exceed the safety threshold γ_{v}, the aviation obstacle is identified as low-risk intruder.

Given the parameters ϕ, θ, R, and v_{r}, the proposed intruder identifier is given in Table I, where γ_R, γ_ϕ, γ_θ, and γ_v are the predefined safety thresholds. The value of these thresholds varies for different classes of UAVs. In Table I, 1 and 0 are used to represent the true and false conditions, respectively, and $X \in \{0, 1\}$. During the SAA procedure, the estimated parameters $\hat{\phi}$, $\hat{\theta}$, $\hat{R}$, and $\hat{v}_{\mathrm{r}}$ are substituted in the classification Table I to identify the risk level of the aviation obstacle. The summary of the proposed SAA method for N_{av} detected aviation obstacles is summarized in Algorithm 1.

TABLE I
Intruder Identification

Multiple hypothesis testing for intruder identification				
Class	$(R < \gamma_{\mathrm{R}})$	$(\lvert\phi - \phi_{\mathrm{v}}\rvert < \gamma_{\phi})$	$(\lvert\theta - \theta_{\mathrm{v}}\rvert < \gamma_{\theta})$	$(v_{\mathrm{r}} > \gamma_{v})$
H_0	1	X	X	X
H_0	0	1	1	1
H_1	0	1	0	1
H_1	0	0	1	1
H_2	0	X	X	0

VIII. SIMULATION

In this section, we evaluate the performance of the proposed estimators and the SAA system under different scenarios.

A. Simulation Setup

Unless otherwise mentioned, the peak power of the DF4 reply by the Mode S transponder of each aviation obstacle is considered to be 8 dBW [28], and it is assumed that the UAV uses two planar antenna arrays with $(N_{\mathrm{x}} = 2) \times (N_{\mathrm{y}} = 2)$ elements, spaced by $d_{\mathrm{x}} = d_{\mathrm{y}} = \lambda/2 = 0.1375$ m in rows and columns, to estimate the azimuth and elevation angles of the aviation obstacles. The elements of the array are backbaffled omnidirectional. The 3-dB beamwidth of the array for the azimuth and elevation angles is $\Delta\phi_3 = \Delta\theta_3 \approx 60^\circ$, and the total number of scans for UF11 Mode S interrogation to cover $\phi \in (0, 180)$ and $\theta \in (-90, 90)$ is $M_{\mathrm{e}}M_{\mathrm{a}} = 9$. The raise and decay time of the Mode S trapezoidal transmit pulse in (5) is $\tau_{\mathrm{r}} = 0.01\mu\mathrm{s}, T = 0.5\,\mu\mathrm{s}$ [23], and $\tau_{\mathrm{gr}} = 270\,\mu s$. The bandwidth of the low-pass filter of root-raised cosine with roll-off factor $\beta = 0.95$ and unit energy $E_{\mathrm{h}} = 1$ at the omnidirectional antenna and the antenna arrays is $B = 6$ MHz [29]. The sampling time at the UAV receiver is $T_{\mathrm{s}} = (1 + \beta)/(2B)$, which results in six samples per PPM symbol and $M = [T/T_{\mathrm{s}}] = 3$. The PSD of the noise N_0 over the filter bandwidth, i.e., $f \in [-B, B]$ is $N_0 = 2.4 \times 10^{-21}$ W/Hz. The maximum time delay to receive the DF4 reply after the transmission of the UF4 Mode S interrogation is $\tau_{\max} = 0.0214$ s. The performance of the proposed estimators is evaluated in terms of RMSE for 10^4 Monte Carlo trials. The simulation setup parameters are summarized in Table II.

B. Simulation Results

Fig. 7 shows the RMSE of the proposed ranging algorithm versus the true range for different values of elevation angle θ for an aviation obstacle. We consider that the azimuth angle and the relative radial velocity of the aviation obstacle and the UAV are distributed as $\phi \in \mathcal{U}_{\mathrm{c}}(0, 180)$ and $v_{\mathrm{r}} = 55$ m/s, respectively. As expected, as the range increases, the RMSE of the proposed ranging algorithm increases. Also, the higher elevation angle $|\theta|$, the lower the RMSE of ranging because of the term $\sin(\hat{\theta})$ in the denominator of the estimator in (33). In terms of bias analysis, the simulation results show that the proposed ranging algorithm is unbiased for $0 < R \leq 10$ km.

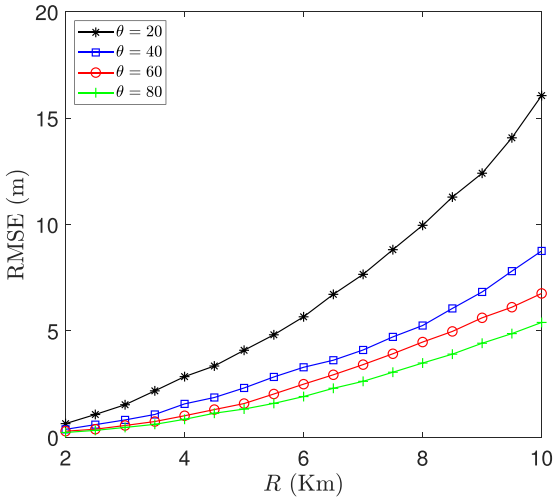

Fig. 7. RMSE of the proposed ranging algorithm for different values of elevation angle θ, $\phi \in \mathcal{U}_{\mathrm{c}}(0, 180)$, and $v_{\mathrm{r}} = 55$ m/s.

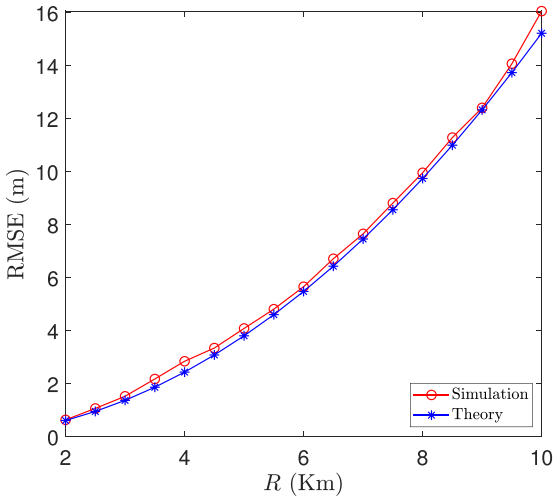

Fig. 8. Theoretical RMSE versus empirical RMSE of the proposed ranging algorithm for $\theta = 20^\circ$.

In Fig. 8, we compare the empirical RMSE of the proposed ranging algorithm obtained by simulation experiments and the theoretical RMSE derived in (35) for different values of R and $\theta = 20^\circ$. As seen, there is a small gap between the empirical RMSE and the theoretical one. The gap between the empirical and the analytical RMSE

Algorithm 1: SAA for N_{av} Aviation Obstacles.

Result: Risk status and navigation parameters of the aviation obstacles, i.e., $\mathcal{R}$ and $\mathcal{P}$

Initialization: $\mathcal{R} = \{\}$ and $\mathcal{P} = \{\}$;
Sense the 1030 MHz radio frequency band using omnidirectional antenna;
if *Channel is not occupied* **then**
  for $m = 1, 2, \ldots, M_{\text{e}} M_{\text{a}}$ **do**
    Transmit UF11 Mode S all-call interrogation for the mth beam space;
    Decode the DF11 relies of the aviation obstacles in the mth beam space
  end
else
  Go to step 2;
end
$N_{\text{av}} \leftarrow$ Number of detected aviation obstacles;
for $k = 1, 2, \ldots, N_{\text{av}}$ **do**
  Send the UF4 roll-call Mode S interrogation for the kth aviation obstacle and wait for its DF4 reply;
  Measure the vector $\mathbf{y}$ and the matrix $\mathbf{Y}$ using the omnidirectional and the antenna array;
  Use $\mathbf{y}$ in (10) to estimate $\hat{n}_k$;
  Use $\mathbf{y}$ and $\hat{n}_k$ in (11) to obtain $\hat{\mathbf{b}}_k$;
  Employ $\hat{\mathbf{b}}_k$ in (14) and obtain $\hat{\mathcal{I}} = \{\hat{i}_0, \hat{i}_1, \ldots, \hat{i}_{i_{55}}\}$;
  Downsample $\mathbf{y}$ as $x_i \triangleq y_{\hat{n}_k + 16M + [M/2] + iM}$ for $i \in \hat{\mathcal{I}}$;
  Obtain $\hat{\boldsymbol{\varphi}} \triangleq \left[\measuredangle x_{\hat{i}_0} \ \measuredangle x_{\hat{i}_1} \ \ldots \ \measuredangle x_{\hat{i}_{55}}\right]^{\text{T}}$;
  Use $\hat{\boldsymbol{\varphi}}$ and $\hat{\boldsymbol{u}} \triangleq \left[\hat{i}_0 \ \hat{i}_1 \ \ldots \ \hat{i}_{55}\right]^{\text{T}}$ in (15) and obtain $\hat{v}_k$;
  Flag=CRC($\hat{\mathbf{b}}_k$);
  Use $\mathbf{Y}$, $\hat{n}_k$, and $\hat{\mathcal{I}}$ to obtain $\mathbf{Y}^{\text{a}}$ in (27);
  Obtain $\hat{\mathbf{A}} = \frac{1}{56M} (\mathbf{Y}^{\text{a}})^{\text{H}} \mathbf{Y}^{\text{a}}$;
  Use the eigenvectors of $\hat{\mathbf{A}}$ in (32) and then solve the maximization problem in (31) to estimate $\hat{\theta}_k$ and $\hat{\phi}_k$;
  if *Flag* $= 1$ **then**
    $\hat{h}_k = \text{Decode}(\hat{\mathbf{b}}_k)$;
    if $|\hat{\theta}_k| > \epsilon_\theta$ **then**
      $\hat{R}_k = (\hat{h}_k - h)/\sin(\hat{\theta}_k)$;
    else
      $\hat{R}_k = \frac{cT_{\text{s}}\hat{n}_k}{2}$;
    end
  else
    $\hat{R}_k = \frac{cT_{\text{s}}\hat{n}_k}{2}$;
  end
  Use $[\hat{R}_k \ \hat{\theta}_k \ \hat{\phi}_k \ \hat{v}_k]^{\text{T}}$ as the input of the intruder identification in Table II and assess the risk status of the kth aviation obstacle S_k;
  $\mathcal{R} \leftarrow \mathcal{R} \cup S_k$;
  $\mathcal{P} \leftarrow \mathcal{P} \cup [\hat{R}_k \ \hat{\theta}_k \ \hat{\phi}_k \ \hat{v}_k]^{\text{T}}$;
end
Return $\mathcal{S}$ and $\mathcal{P}$

TABLE II
Simulation Setup Parameters

Parameter	Unit	Value
P_{t}	dB·W	8
B	MHz	6
T	μs	0.5
τ_{r}	μs	0.01
τ_{gr}	μs	270
$\tau_{\max}$	ms	21.4
$\Delta\phi_3$	Degree	60
$\Delta\theta_3$	Degree	60
N_0	W/Hz	2.4×10^{-21}
d_{x}	m	0.1375
d_{y}	m	0.1375
N_{a}	-	4
N_{x}	-	2
N_{y}	-	2
M	-	3
ϵ_θ	Degree	1

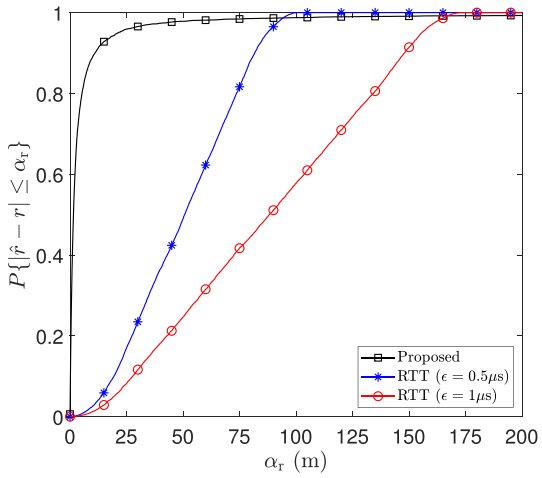

Fig. 9. Range error probability comparison of the proposed ranging algorithm with the RTT-based ranging algorithm.

decreases as the number of PPM symbols increases by receiving multiple DF4 replies or by using extended-length DF4 downlink replies.

Fig. 9 compares the range error probability of the RTT-based and the proposed ranging algorithms. The range error probability is defined as $\mathbb{P}\{|\hat{r} - r| \leq \alpha_{\text{r}}\}$, and it is assumed that the azimuth and elevation angles of the aviation obstacle are $\phi \in \mathcal{U}_{\text{c}}(0, 180)$ and $|\theta| \in \mathcal{U}_{\text{c}}(1, 90)$, respectively, and the relative radial velocity of the UAV is $v_{\text{r}} = 55$ m/s. For the RTT-based ranging algorithm, we consider that there is $r_\epsilon \sim \mathcal{U}_{\text{c}}(0, \epsilon)$ random delay in the response of the Mode S transponder. As seen, the proposed ranging algorithm outperforms the RTT-based ranging algorithm even for small values of ϵ.

Fig. 10 illustrates the RMSE of the proposed Doppler frequency shift estimator for $-600 \leq f_{\text{D}} \leq 600$ Hz and different values of the range R. We consider that the elevation and azimuth angles of the aviation obstacle are distributed as $\phi \in \mathcal{U}_{\text{c}}(0, 180)$ and $|\theta| \in \mathcal{U}_{\text{c}}(1, 90)$. We also show the theoretical RMSE derived in (20). As seen, the proposed estimator offers low RMSE at high SNR values. Moreover,

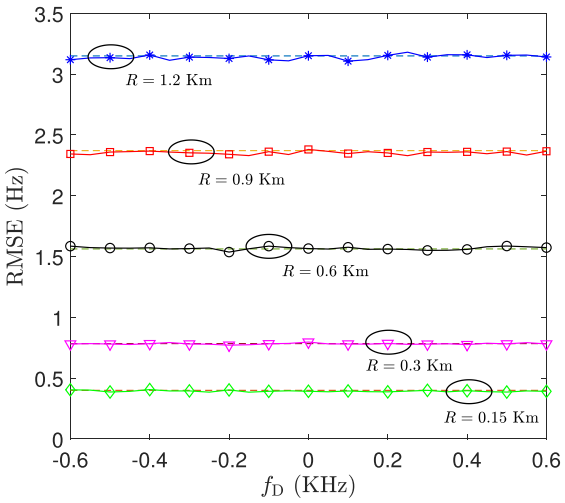

Fig. 10. RMSE of the proposed Doppler frequency shift estimator for different values of R. The dashed line shows the theoretical RMSE.

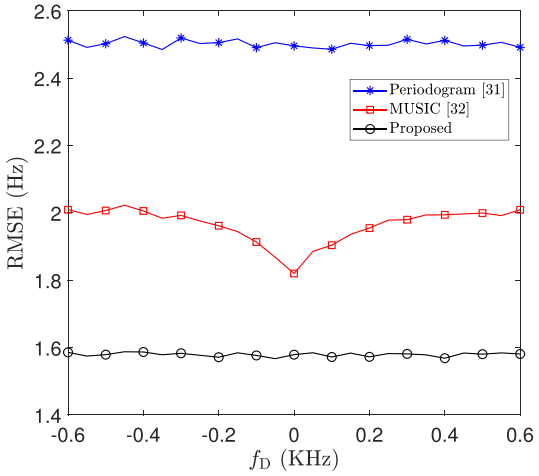

Fig. 11. Performance comparison of the proposed Doppler frequency shift estimator with the periodogram and the MUSIC estimators.

the RMSE obtained by simulation experiments matches the theoretical RMSE.

In Fig. 11, we compare the RMSE of the proposed Doppler frequency shift estimator with the periodogram estimator in [30] and the MUSIC estimator in [31]. The azimuth and elevation angles of the aviation obstacle are assumed to be $\phi \in \mathcal{U}_c(0, 180)$ and $|\theta| \in \mathcal{U}_c(1, 90)$, respectively, and the range between the UAV and the aviation obstacle is $R = 0.6$ Km. As seen, the proposed Doppler frequency shift estimator outperforms the MUSIC and the periodogram estimators with lower computational complexity. The complexity order of the proposed Doppler frequency shift estimator, the Lomb–Scargle periodogram, and the MUSIC are $\mathcal{O}(N_e^2)$, $\mathcal{O}(N_e F)$ [32], and $\mathcal{O}(N_a^3 + N_a^2 N_e + F)$ [33], respectively, where N_a is the number of array elements, F is the number of frequency grids, and N_e is the number of observation samples used for estimation.

In Fig. 12, we evaluate the performance of the intruder identification method developed using the proposed range and RV-Es. Without loss of generality, we consider

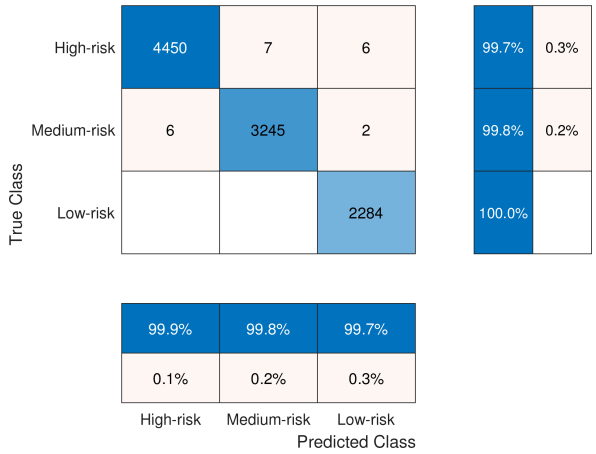

Fig. 12. Performance of the proposed intruder identification method for 10^4 Monte Carlo trials.

that the movement direction of the UAV is $\phi_v = 0^\circ$ and $\theta_v = 0^\circ$ in the coordinates of the array. For eight aviation obstacles in the airspace, we assume that $\phi \in \mathcal{U}_c(0, 180)$, $|\theta| \in \mathcal{U}_c(1, 90)$, and $R \in \mathcal{U}_c(0.1, 1)$ km. The relative radial velocity of the aviation obstacle and the UAV is assumed to be $v_r \in \mathcal{U}_c(-139, +139)$ m/s. The safety thresholds in Table II are considered to be $\lambda_R = 0.5$ km, $\lambda_\phi = 10^\circ$, $\lambda_\theta = 10^\circ$, and $\lambda_v = 20$ m/s. The safety parameter associated with the radial velocity $\lambda_v = 20$ m/s gives 25 s time to the UAV to avoid any possible collision with the aviation obstacle. As seen in Fig. 12, the proposed intruder identification mechanism can accurately classify the aviation obstacles. High-risk intruders can be identified with a probability of 0.997, which is significant.

IX. CONCLUSION

A cooperative RF-based SAA algorithm for the safe navigation of small-sized UAVs was proposed in this article. The proposed SAA algorithm takes the advantage of the Mode S SSR like the ACAS; however, it is capable of radial velocity estimation using a single DF4 reply. In addition, it uses a new ranging algorithm based on the triangular relation between the estimated elevation angle and the altitude difference between the aviation obstacle and the UAV. The proposed triangulation-based ranging algorithm is more accurate compared to the RTT-based ranging algorithm, and their combination is a promising solution for high accuracy ranging. The proposed SAA system benefits from an intruder identification mechanism that can accurately identify the risk level of the aviation obstacles in the airspace. Future work will explore the applicability of the proposed SAA for industrial aircraft, the evaluation of the proposed SAA with real data, the development of channel access for the simultaneous detection of multiple UAVs, and the combination of 5 G technologies and SSR.

APPENDIX A

Let n_0 denote the index of the first sample of the DF4 reply received in the UAV omnidirectional antenna receiver. The index of the sample denoting the start of the payload

symbols is $n_s \triangleq n_0 + 16M$. We can write the $K \triangleq 112M$ observation samples corresponding to the payload PPM vector $\bar{\mathbf{b}} = [\bar{b}_0\, \bar{b}_1\, \ldots\, \bar{b}_{111}]^{\mathrm{T}} = [b_0\, \neg b_0\, b_1\, \neg b_1\, \ldots\, b_{55}\, \neg b_{55}]^{\mathrm{T}}$, i.e., $y_{n_0+16M}, y_{n_0+16M+1}, \ldots, y_{n_0+16M+K-1}$ as

$$\mathbf{a} = \begin{bmatrix} a_0\, a_1\, \ldots\, a_{K-1} \end{bmatrix}^{\mathrm{T}} \approx \frac{\sqrt{P_t \eta_0}}{L} \mathbf{F}_s (\bar{\mathbf{b}} \otimes \mathbf{g}) + \mathbf{v}_s \tag{38}$$

where $a_k \triangleq y_{n_0+16M+k}$, $\mathbf{F}_s \triangleq \mathrm{diag}(\mathbf{f}_s)$,

$$\mathbf{f}_s \triangleq \Big[e^{j(2\pi f_D T_s n_s + \psi_0)}\, e^{j(2\pi f_D T_s (n_s+1) + \psi_0)} \ldots\, e^{j(2\pi f_D T_s (K+n_s-1) + \psi_0)} \Big]^{\mathrm{T}} \tag{39}$$

$\mathbf{v}_s \triangleq [w_{n_s}\, w_{n_s+1}\, \ldots\, w_{n_s+K-1}]^{\mathrm{T}}$, and $\mathbf{g} = [g_0\, g_1\, \ldots\, g_{M-1}]^{\mathrm{T}}$. To estimate the Doppler frequency shift, we can use the M-fold decimation of $\mathbf{a}$ as

$$\mathbf{x} = \begin{bmatrix} x_0\, x_1\, \ldots\, x_{111} \end{bmatrix}^{\mathrm{T}} = \begin{bmatrix} a_{n_c}\, a_{n_c+M}\, \ldots\, a_{n_c+111M} \end{bmatrix}^{\mathrm{T}} \approx \frac{\sqrt{P_t \eta_0}}{L} g_{n_c} \mathbf{F}_d \bar{\mathbf{b}} + \mathbf{v}_d \tag{40}$$

where $n_c \triangleq [M/2]$, $\mathbf{F}_d \triangleq \mathrm{diag}(\mathbf{f}_d)$,

$$\mathbf{f}_d \triangleq \Big[e^{j(2\pi f_D T_s n_d + \psi_0)}\, e^{j(2\pi f_D T_s (n_d+M) + \psi_0)} \ldots\, e^{j(2\pi f_D T_s (n_d+111M) + \psi_0)} \Big]^{\mathrm{T}} \tag{41}$$

and $\mathbf{v}_d \triangleq \begin{bmatrix} w_{n_d}\, w_{n_d+M}\, \ldots\, w_{n_d+111M} \end{bmatrix}^{\mathrm{T}}$, with $n_d \triangleq n_s + n_c = n_0 + 16M + [M/2]$. g_{n_c}, $n_c \triangleq [M/2]$, is the (n_c+1)th elements of the pulse shaping vector $\mathbf{g}$ given in (7e). The vector $\mathbf{x}$ is obtained by sampling in the middle of the received pulses.

At moderately high SNR values that is the case in SAA systems, the signal model in (40) can be approximated by [34]

$$x_i = y_{n_d+iM} = y_{n_0+M(16+i)+n_c} = y_{n_0+M(16+i)+[\frac{M}{2}]} \approx \frac{\sqrt{P_t \eta_0}}{L} g_{n_c} e^{j(2\pi f_D T_s (n_d+iM) + \psi_0 + \vartheta_i)}, \quad i \in \mathcal{I} \tag{42}$$

where the set $\mathcal{I}$ with cardinality $|\mathcal{I}| = 56$ is given in (14), $\vartheta_i \in \mathbb{R}$, $i \in \mathcal{I}$, is zero-mean white Gaussian noise with variance $\sigma_\vartheta^2 = \frac{1}{2}(L^2 \sigma_w^2)/(P_t \eta_0 g_{n_c})$. The phase of x_i can be written as

$$\measuredangle x_i = \measuredangle y_{n_d+iM} \approx 2\pi f_D T_s (n_d + iM) + \psi_0 + \vartheta_i, \quad i \in \mathcal{I}. \tag{43}$$

The Doppler frequency shift between the UAV and the aviation obstacle f_D can be estimated by the phase of the received signal in (43). Let us write the phase difference of the received signal in (43) in vector form as

$$\boldsymbol{\Delta\varphi} = 2\pi M f_D T_s \boldsymbol{\Delta u} + \boldsymbol{\Delta\vartheta} \tag{44}$$

where $\boldsymbol{\varphi} \triangleq \begin{bmatrix} \measuredangle x_{i_0}\, \measuredangle x_{i_1}\, \ldots\, \measuredangle x_{i_{55}} \end{bmatrix}^{\mathrm{T}}$, $\boldsymbol{u} \triangleq \begin{bmatrix} i_0\, i_1\, \ldots\, i_{55} \end{bmatrix}^{\mathrm{T}}$, $\boldsymbol{\vartheta} \triangleq \begin{bmatrix} \vartheta_{i_0}\, \vartheta_{i_1}\, \ldots\, \vartheta_{i_{55}} \end{bmatrix}^{\mathrm{T}}$, $i_k \in \mathcal{I}$ and $i_0 < i_1 < \ldots < i_{55}$, and $\boldsymbol{\Delta}$ is the 55×56 discrete derivative matrix given in (17). We can easily show that for PPM signaling, we have $i_{k+1} - i_k \in \{1, 2, 3\}$ for $i_k \in \mathcal{I}$.

Because $\boldsymbol{\vartheta} \sim \mathcal{N}(0, \sigma_\vartheta^2 \mathbf{I})$, the noise vector $\boldsymbol{\Delta\vartheta} = [\vartheta_{i_0} - \vartheta_{i_1}\ \vartheta_{i_1} - \vartheta_{i_2}\ \ldots\ \vartheta_{i_{54}} - \vartheta_{i_{55}}]^{\mathrm{T}}$ in (44) is zero-mean and colored with covariance matrix $\mathbf{C}$, where the entry on the mth row and nth column of the covariance $\mathbf{C}$, i.e., $C_{mn} = \mathbb{E}\{(\vartheta_{i_{(m-1)}} - \vartheta_{i_m})(\vartheta_{i_{(n-1)}} - \vartheta_{i_n})\}$ is given by

$$\mathbf{C}_{mn} = \sigma_\vartheta^2 \begin{cases} 2 & m = n \\ -1 & m \in \{n-1, n+1\} \\ 0 & \text{otherwise.} \end{cases} \tag{45}$$

Using [35, eqs. (7-43) and (7-44)], the optimal maximum likelihood estimation of the Doppler frequency shift, f_D, and its RMSE for the linear observation model in (44) are obtained as in (15) and (20), respectively. Since $\mathbb{E}\{\boldsymbol{\Delta\vartheta}\} = \mathbf{0}_{55}$, we have $\mathbb{E}\{\boldsymbol{\Delta\varphi}\} = 2\pi M f_D T_s \boldsymbol{\Delta u}$, and thus, we can write

$$\mathbb{E}\{\hat{f}_D\} = \frac{1}{2\pi M T_s} \frac{\mathbf{u}^{\mathrm{T}} \boldsymbol{\Delta}^{\mathrm{T}} \mathbf{C}^{-1} \mathbb{E}\{\boldsymbol{\Delta\varphi}\}}{\mathbf{u}^{\mathrm{T}} \boldsymbol{\Delta}^{\mathrm{T}} \mathbf{C}^{-1} \boldsymbol{\Delta u}} = f_D \tag{46}$$

which shows that the proposed Doppler frequency shift estimator is an unbiased estimator.

APPENDIX B

Let the sequence $\{\mathrm{PRI}_1, \mathrm{PRI}_2, \ldots, \mathrm{PRI}_Q\}$, $Q \in \mathbb{N}$, denote the PRI group of a pulse radar, where $\mathrm{PRI}_i \triangleq \frac{a_i}{b_i}$, and a_i and b_i are coprime integers. The maximum unambiguous Doppler frequency shift of this waveform is given by [36]

$$|f_D| \le \frac{\mathrm{LCM}(b_1, b_2, \ldots, b_Q)}{\mathrm{GCD}(a_1, a_2, \ldots, a_Q)} \tag{47}$$

where LCM and GCD denote the least common multiple and the greatest common devisor, respectively. For the DF4 PPM waveform with $T = 0.5\mu$s, we have $\mathrm{PRI}_i \triangleq \frac{a_i}{b_i} \in \{T, 2T, 3T\} = \{\frac{1}{2\times 10^6}, \frac{1}{10^6}, \frac{3}{2\times 10^6}\}$. Hence, we can write

$$|f_D| = \le \frac{\mathrm{LCM}(b_1, b_2, \ldots, b_Q)}{\mathrm{GCD}(a_1, a_2, \ldots, a_Q)} = \frac{\mathrm{LCM}(2\times 10^6, 10^6, 2\times 10^6)}{\mathrm{GCD}(1, 1, 3)} = 2\times 10^6 = \frac{1}{T}. \tag{48}$$

Finally, by substituting (48) into $|f_D| = \frac{|v_r|}{\lambda}$, we obtain (22).

APPENDIX C

Here, we exploit the results in [37] to analytically obtain the asymptotic MSE of the 2D-MUSIC for the planar antenna array used in the proposed SAA system. By defining $\omega_\theta \triangleq \sin(\theta)$, $\cos(\theta) = \sqrt{1-\omega_\theta^2}$, and exploiting the result of [37, eq. (3.14)], we asymptotically obtain the 2D-MUSIC estimation error of $\hat{\omega}_\theta = \sin(\hat{\theta})$ as

$$\mathbb{E}\big\{(\hat{\omega}_\theta - \omega_\theta)^2\big\} = \frac{\frac{\sigma_w^2}{112M} \frac{\lambda_{\max}}{(\sigma_w^2 - \lambda_{\max})^2} \big|\mathbf{a}^{\mathrm{H}}(\theta, \phi)\mathbf{e}_1\big|^2}{\sum_{n=2}^{N_a} \big|\boldsymbol{\alpha}^{\mathrm{H}}(\theta, \phi)\mathbf{e}_n\big|^2} \tag{49}$$

where $\boldsymbol{\alpha}(\theta, \phi) \triangleq \big[\alpha_{1,1}(\theta, \phi)\, \alpha_{2,1}(\theta, \phi)\ \ldots\ \alpha_{N_x, N_y}(\theta, \phi)\big]^{\mathrm{T}}$ with $\alpha_{m,n}(\theta, \phi)$ in (36), and $a_{m,n}(\theta, \phi)$ is given in (30). In (49), the vector $\mathbf{e}_1$ is the eigenvector corresponding to the largest eigenvalue of $\Lambda \triangleq \xi \mathbf{a}^*(\theta, \phi)\mathbf{a}^{\mathrm{T}}(\theta, \phi) + \sigma_w^2 \mathbf{I}$, i.e.,

$\lambda_{\max}$, $\mathbf{e}_k$, $k = 2, 3, \ldots, N_x N_y$ are the eigenvectors corresponding to the $N_x N_y - 1$ eigenvalues $\lambda = \sigma_w^2$, and ξ is given in (37).

Similarly, by defining $\omega_\phi \triangleq \sin(\phi)$, and exploiting the result of [37, eq. (3.12)], we obtain the asymptotic 2D-MUSIC estimation error for $\hat{\omega}_\phi = \sin(\hat{\phi})$ as

$$\mathbb{E}\left\{(\hat{\omega}_\phi - \omega_\phi)^2\right\} = \frac{\frac{\sigma_w^2}{112M}\frac{\lambda_{\max}}{(\sigma_w - \lambda_{\max})^2}\left|\mathbf{a}^{\mathrm{H}}(\theta,\phi)\mathbf{e}_1\right|^2}{\sum_{n=2}^{N_a}\left|\boldsymbol{\beta}^{\mathrm{H}}(\theta,\phi)\mathbf{e}_n\right|^2} \tag{50}$$

where $\boldsymbol{\beta}(\theta,\phi) \triangleq \left[\beta_{1,1}(\theta,\phi)\ \beta_{2,1}(\theta,\phi)\ \ldots\ \beta_{N_x,N_y}(\theta,\phi)\right]^{\mathrm{T}}$ with $\beta_{m,n}(\theta,\phi)$ as

$$\begin{aligned}\beta_{m,n}(\theta,\phi) &\triangleq \frac{\partial a_{m,n}(\theta,\phi)}{\partial \sin(\phi)} \\ &= \frac{j2\pi}{\lambda} d_y (n-1)\sin(\theta) a_{m,n}(\theta,\phi).\end{aligned} \tag{51}$$

Similar to [37], we can show that $\hat{\omega}_\theta - \omega_\theta$ and $\hat{\omega}_\phi - \omega_\phi$ are asymptotically jointly Gaussian distribution with zero mean.

APPENDIX D

Stoica and Nehorai [37] proved that $\hat{\omega}_\theta$ is asymptotically an unbiased estimate of $\omega_\theta = \sin(\theta)$. Thus, we can write $\hat{\omega}_\theta = \sin(\hat{\theta}) = \sin(\theta) + Z$, where $Z \sim \mathcal{N}(0, \mu)$ and $\mu \triangleq \mathbb{E}\left\{(\hat{\omega}_\theta - \omega_\theta)^2\right\}$ is given in (49). By defining $X \triangleq Z/\omega_\theta$ (for moderately high SNR values and sufficiently large $|\epsilon_\theta|$, we have $\mathbb{P}\{|X| < 1\} \approx 1$) and using the series representations $\frac{1}{1+X} = \sum_{n\geq 0}(-1)^n X^n$, $|X| < 1$, for $|\theta| > \epsilon_\theta$, we can write

$$\begin{aligned}\hat{R} &= \frac{h_a - h}{\sin(\hat{\theta})} = \frac{h_a - h}{\sin(\theta) + Z} \\ &= (h_a - h)\sum_{n\geq 0}(-1)^n \frac{Z^n}{(\sin(\theta))^{n+1}} \\ &= \frac{(h_a - h)}{\sin(\theta)}\left(1 - \frac{Z}{\sin(\theta)} + \mathcal{O}\left(\frac{Z^2}{(\sin(\theta))^2}\right)\right), \frac{Z}{\sin(\theta)} \to 0\end{aligned} \tag{52}$$

where h and h_a denote the altitude of the UAV and the aviation obstacle, respectively. The series in (52) converges by the ratio test if $|Z| < |\sin(\theta)|$ and $|\theta| \geq \epsilon_\theta$.

For moderately high SNR values and $|\theta| \geq \epsilon_\theta$, $Z/\sin(\theta) \to 0$; hence, by taking expectations on both sides of (52), we obtain

$$\mathbb{E}\{\hat{R}\} = \mathbb{E}\left\{\frac{h_a - h}{\sin(\hat{\theta})}\right\} \approx \frac{h_a - h}{\sin(\theta)}. \tag{53}$$

The variance of $\{\hat{R}\}$ is also given by

$$\mathrm{var}\{\hat{R}\} = \mathrm{var}\left\{\frac{h_a - h}{\sin(\hat{\theta})}\right\} \approx \frac{(h_a - h)^2 \mathrm{var}\{Z\}}{\sin^4(\theta)}. \tag{54}$$

Because $\mathbb{E}\{\hat{R}\} \approx R$, the MSE of the estimated range of the aviation obstacle is given by

$$\mathbb{E}\{(\hat{R} - R)^2\} \approx \frac{(h_a - h)^2 \mathrm{var}\{Z\}}{\sin^4(\theta)}. \tag{55}$$

Finally, by replacing $\mathrm{var}\{Z\}$ with $\mathbb{E}\left\{(\hat{\omega}_\theta - \omega_\theta)^2\right\}$ in (49), we obtain (35).

REFERENCES

[1] J.-H. Son, S. Choi, and J. Cha, "A brief survey of sensors for detect, sense, and avoid operations of small unmanned aerial vehicles," in *Proc. 17th Int. Conf. Control, Automat. Syst.*, 2017, pp. 279–282.

[2] F. Tomasello and D. Haddon, "Detect and avoid for unmanned aircraft systems in the total system approach," in *Proc. IEEE Tyrrhenian Int. Workshop Digit. Commun.—Enhanced Surveill. Aircr. Veh.*, 2011, pp. 47–52.

[3] G. Fasano, D. Accado, A. Moccia, and D. Moroney, "Sense and avoid for unmanned aircraft systems," *IEEE Aerosp. Electron. Syst. Mag.*, vol. 31, no. 11, pp. 82–110, Nov. 2016.

[4] J. McCalmont, J. Utt, and M. Deschenes, "Detect and avoid technology demonstration," in *Proc. 1st UAV Conf.*, 2002, Art. no. 3419.

[5] H. Lyu et al., "Detect and avoid system based on multi sensor fusion for UAV," in *Proc. IEEE Int. Conf. Inf. Commun. Technol. Convergence*, 2018, pp. 1107–1109.

[6] X. Yu and Y. Zhang, "Sense and avoid technologies with applications to unmanned aircraft systems: Review and prospects," *Prog. Aerosp. Sci.*, vol. 74, pp. 152–166, 2015.

[7] Y. A. Nijsure, G. Kaddoum, N. K. Mallat, G. Gagnon, and F. Gagnon, "Cognitive chaotic UWB-MIMO detect-avoid radar for autonomous UAV navigation," *IEEE Trans. Intell. Transp. Syst.*, vol. 17, no. 11, pp. 3121–3131, Nov. 2016.

[8] C. Ben, M. Keller, N. Voget, and D. Moormann, "Evaluation of a radar based three-dimensional detect and avoid system for small unmanned aerial systems," in *Proc. IEEE 17th AIAA Aviation Technol., Integr., Operations Conf.*, 2017, pp. 4386–4397.

[9] E. Aldao, L. M. González-de Santos, and H. González-Jorge, "Lidar based detect and avoid system for UAV navigation in UAM corridors," *MDPI Drones*, vol. 6, no. 8, 2022, Art. no. 185.

[10] V. A. Orlando, "The mode S beacon radar system," *Lincoln Lab. J.*, vol. 2, no. 3, pp. 345–362, 1989.

[11] M. Smith, M. Strohmeier, V. Lenders, and I. Martinovic, "Understanding realistic attacks on airborne collision avoidance systems," *J. Transp. Secur.*, vol. 15, no. 1-2, pp. 87–118, 2022.

[12] P. M. Berges, B. A. Shivakumar, T. Graziano, R. Gerdes, and Z. B. Celik, "On the feasibility of exploiting traffic collision avoidance system vulnerabilities," in *Proc. IEEE Conf. Commun. Netw. Secur.*, 2020, pp. 1–6.

[13] Y. Lin and S. Saripalli, "Sense and avoid for unmanned aerial vehicles using ADS-B," in *Proc. IEEE Int. Conf. Robot. Automat.*, 2015, pp. 6402–6407.

[14] R. K. Barnhart, D. M. Marshall, and E. Shappee, *Introduction to Unmanned Aircraft Systems*. Boca Raton, FL, USA: CRC Press, 2021.

[15] P. Angelov, *Sense and Avoid in UAS: Research and Applications*. Hoboken, NJ, USA: Wiley, 2012.

[16] W. Semke et al., "Analysis of radar and ADS-B influences on aircraft detect and avoid (DAA) systems," *MDPI Aerosp.*, vol. 4, no. 3, 2017, Art. no. 49.

[17] M. Strohmeier, M. Schäfer, V. Lenders, and I. Martinovic, "Realities and challenges of nextgen air traffic management: The case of ADS-B," *IEEE Commun. Mag.*, vol. 52, no. 5, pp. 111–118, May 2014.

[18] J. Kuchar and A. C. Drumm, "The traffic alert and collision avoidance system," *Lincoln Lab. J.*, vol. 16, no. 2, 2007, Art. no. 277.

[19] L. R. Sahawneh, M. O. Duffield, R. W. Beard, and T. W. McLain, "Detect and avoid for small unmanned aircraft systems using ADS-B," *Air Traffic Control Quart.*, vol. 23, no. 2-3, pp. 203–240, 2015.

[20] B. Torvik, K. E. Olsen, and H. Griffiths, "Classification of birds and UAVs based on radar polarimetry," *IEEE Geosci. Remote Sens. Lett.*, vol. 13, no. 9, pp. 1305–1309, Sep. 2016.

[21] C. C. M. Kyba et al., "High-resolution imagery of earth at night: New sources, opportunities and challenges," *Remote Sens.*, vol. 7, no. 1, pp. 1–23, 2015.

[22] J. Sun, *The 1090 megahertz Riddle: A Guide to Decoding Mode S and ADS-B Signals*. Delft, Netherlands: TU Delft OPEN Publishing, 2021.
[23] M. Leonardi, L. Di Gregorio, and D. Di Fausto, "Air traffic security: Aircraft classification using ADS-B message's phase-pattern," *MDPI Aerosp.*, vol. 4, no. 4, pp. 1–13, 2017.
[24] A. Normalien, *Algorithms for Separation of Secondary Surveillance Radar Replies*, Lyon, France: Ecole Normale Superieure de Lyon OPEN Publishing, 2002.
[25] M. Marcus, *Basic Theorems in Matrix Theory*. Washington, DC, USA: U.S. Government Printing Office, 1948.
[26] H. L. Van Trees, *Optimum Array Processing: Part IV of Detection, Estimation, and Modulation Theory*. Hoboken, NJ, USA: Wiley, 2002.
[27] S. g. Woo, C. Park, D. Lee, and S.-y. Lee, "Collision avoidance for unmanned aerial vehicles based on safety radius of the formation geometry," in *Proc. IEEE 20th Int. Conf. Control, Automat. Syst.*, 2020, pp. 179–183.
[28] J. Berends and E. Potier, "Considerations for low power SSR Mode-S transponder (LPST) operations," European Organisation for the Safety of Air Navigation, Oct. 2007.
[29] "*Airplane Tracking Using ADS-B Signals*," Sep. 30, 2010. [Online]. Available: https://www.mathworks.com/help//comm/ug/airplane-tracking-using-ads-b-signals.html
[30] S. A. Fulop and K. Fitz, "Algorithms for computing the time-corrected instantaneous frequency (reassigned) spectrogram, with applications," *J. Acoustical Soc. Amer.*, vol. 119, no. 1, pp. 360–371, 2006.
[31] P. Stoica et al. in *Spectral Analysis of Signals*, vol. 452. Upper Saddle River, NJ, USA: Prentice-Hall, 2005.
[32] N. R. Lomb, "Least-squares frequency analysis of unequally spaced data," *Astrophys. Space Sci.*, vol. 39, pp. 447–462, 1976.
[33] E. Gentilho Jr, P. R. Scalassara, and T. Abrão, "Direction-of-arrival estimation methods: A performance-complexity tradeoff perspective," *J. Signal Process. Syst.*, vol. 92, no. 2, pp. 239–256, 2020.
[34] S. Tretter, "Estimating the frequency of a noisy sinusoid by linear regression (corresp.)," *IEEE Trans. Inf. Theory*, vol. 31, no. 6, pp. 832–835, Nov. 1985.
[35] S. M. Kay, *Fundamentals of Statistical Signal Processing: Estimation Theory*. Englewood Cliffs, NJ, USA: Prentice-Hall., 1993.
[36] Y. Lu, Z. Tang, Y. Zhang, and L. Yu, "Maximum unambiguous frequency of random PRI radar," in *Proc. CIE Int. Conf. Radar*, Oct. 2016, pp. 1–5.
[37] P. Stoica and A. Nehorai, "MUSIC, maximum likelihood, and cramer-rao bound," *IEEE Trans. Acoust., Speech, Signal Process.*, vol. 37, no. 5, pp. 720–741, May 1989.